EXPERIMENTAL AND THEORETICAL INVESTIGATIONS OF THE DECAYS OF ^{206}Fr AND ^{208}Fr

by

Barry Graham Ritchie

Bachelor of Science
Appalachian State University, 1975

Master of Science
University of South Carolina, 1977

Submitted in Partial Fulfillment of the Requirements

for the Degree of Doctor of Philosophy in the

Department of Physics and Astronomy

University of South Carolina

1979

Frank T. Avignone III
Major Professor
Chairman, Examining Committee

Eugene H. Spejewski
Committee Member

James M. Knight
Committee Member

H. K. Carter
Committee Member

Barry Blanpied
Committee Member

J. H. Wahab
Committee Member

Dean of the Graduate School

ACKNOWLEDGMENTS

I wish to thank Oak Ridge Associated Universities and the U.S. Department of Energy for the financial support provided by them throughout my appointment as a Laboratory Graduate Participant at UNISOR.

I also wish to thank the many Oak Ridge National Laboratory/ Physics Division personnel who assisted me during my two-year stay there. I particularly wish to thank Dr. K. S. Toth for his advice and consultations on several phases of this project. Much gratitude is offered also to Drs. M. A. Grimm and J. D. Cole for their help and friendship.

I thank the members of my committee for reviewing my dissertation, and Ms. Martha M. Dawson for typing much of it.

An important personal milestone is rarely achieved without some help from others. In my case, much of that help has been invaluable. In particular, I wish to thank the following people:

-Mrs. Dorothy Helms and Mrs. Mary Johnston for getting me started on this path;

-Drs. W. C. Connolly, J. G. Lindsay, K. C. Mamola, R. C. Nicklin, and T. L. Rokoske for their guidance and personal interest in me during my undergraduate study.

- Dr. F. T. Avignone, III, for his support, tutorage, and direction (tempered with a fair amount of patience) as my advisor throughout my years of graduate school;

-Dr. R. L. Mlekodaj, for suggesting this project and willingly serving as an erstwhile consultant on the subjects contained herein (as well as many not quite so serious) during the past two years;

-Dr. E. H. Spejewski, for prodding, suggesting and encouraging my work at UNISOR, putting its resources at the disposal of a very thankful graduate student;

-Dr. H. K. Carter, who took me "under his wing" at UNISOR, urging, guiding and supporting me with a strong personal interest, answering hundreds of questions, and carefully supervising my project from conception to the final draft of this work "above and beyond the call of duty";

-my parents, Mr. and Mrs. Price E. Ritchie, who unswervingly supported and trusted me over two decades of education, and to whom I owe a lifetime of gratitude; and

-most of all, my wife, Romell, who has provided an inexhaustible source of all kinds of support--personal, logistical, and, of course, financial. Her faith and trust in me have provided a firm base for my ventures for nearly ten years. As a small mark against a tremendous debt of gratitude, I dedicate this work to her.

TABLE OF CONTENTS

LIST OF TABLES

LIST OF FIGURES

ABSTRACT

The decays of ^{206}Fr and ^{208}Fr, produced by bombarding natural iridium with 110-120 MeV ^{20}Ne, have been studied. The nuclei were mass separated at the UNISOR facility and observed with large volume semiconductor detectors in calibrated geometries. Alpha, gamma, and electron singles and gamma-gamma and gamma-electron coincidence data have been taken. Special procedures have been used to determine alpha and gamma ray energies to high accuracy.

The alpha decay experiments have permitted the determination of the alpha branching ratios for ^{206,208}Fr as well as ^{205,207}Fr. The method used includes the information obtained from the electron capture decay studies of those nuclei. Such a method requires no a priori knowledge of daughter branching ratios, which is a major difference from previous measurements by other groups. The alpha branching ratios obtained are generally higher than those reported previously. Energies and half-lives are in general agreement with previous measurements.

The alpha measurements also have revealed the presence of a heretofore unobserved alpha-emitting isomer in ^{206}Fr. The isomer has a half-life of 0.7 ± 0.1 seconds, and the energy of the associated alpha decay is 6.930 ± 0.005 MeV. Gamma data taken with the alpha measurements suggest that the isomeric level is 531 keV above the ^{206}Fr ground state, with the associated alpha decay populating a level at 391 keV in the ^{202}At nucleus.

The measured alpha branching ratios were analyzed using the Rasmussen reduced width formalism. Angular momentum transfer in the decays were taken into account by the calculations. The calculated reduced widths were compared to those for the radium and radon nuclei, which are assumed to represent unhindered alpha decays. All observed francium decays were deduced to be unhindered.

No studies of the electron capture decays of ^{206,208}Fr have been performed previously. The studies performed here have produced detailed level schemes for ^{206}Rn and ^{208}Rn. The gamma and electron data have permitted the determination of internal conversion coefficients and, consequently, multipolarities for many of the transitions within the radon nuclei. These, in turn, have allowed the deduction of unique spins and parities for many of the levels within the two nuclei and the deduction of ranges for other levels.

The deduced level schemes have been correlated with previous in-beam work on the neutron deficient radon isotopes. It appears from these systematics that two different bands of states above $J^{\pi} = 4+$ are populated by in-beam studies. The states populated by in-beam experiments on ^{208}Rn do not include the 4+ yrast level of that nucleus in the cascade but instead populate a higher energy 4+ level. The ^{208}Rn level scheme is suggestive of a rotational-like side band which may support explanations of this phenomenon in terms of band crossing.

The deduced level scheme of ^{208}Rn has been studied using the interacting boson approximation (IBA) with the computer code PHINT. The level scheme is readily explained with this model up to around 2 MeV. Good agreement between theory and experiment has also been obtained for ^{204}Rn and ^{206}Rn, but the limited detail in these decay schemes do

not provide conclusive evidence for the applicability of the IBA to the ^{204}Rn and ^{206}Rn nuclei.

CHAPTER 1

INTRODUCTION

Nuclei which possess a few nucleons outside a doubly magic nucleus such as ^{208}Pb are of great interest to nuclear physicists. The observed nuclear properties yield clues to the form of the nucleon-nucleon interaction and the ability of collective models to describe such nuclei. Much experimental and theoretical work has been performed in the regions around doubly magic nuclei to obtain as detailed a description of these nuclei as possible.

An important method for analyzing the nuclei in a region is to observe systematic trends in the level structures as pairs of nucleons are added. Such trends allow interpretation of the states in terms of their underlying collective structure. To adequately perform such an analysis, however, the level schemes should be known in some detail. Hence a series of experiments might be performed for just this purpose.

There are several isotopic series near doubly magic ^{208}Pb where little detailed information exists. One such series is the neutron deficient ($N < 126$) radon nuclei. These isotopes have four protons outside the closed proton shell at $Z = 82$ and represent nuclear situations still tractable in terms of calculations based on the shell model with model nucleon-nucleon interactions. With the successive addition of neutron holes, these nuclei also present opportunities for investigating the onset of collective behavior with nuclear models employing

collective rather than single-particle degrees of freedom. This is particularly true for the even-even nuclei, since many collective models exist for them.

The neutron deficient radon nuclei can be studied by in-beam spectroscopy with (heavy ion, xnγ) reactions or by observing decays to their levels following (heavy ion, xn) reactions creating parent nuclei which decay to the radon isotopes. These two different methods provide complementary techniques for exploring different facets of the nuclear level structures.

In-beam spectroscopy studies observe the electromagnetic decay of the produced nuclei from highly excited, high angular momentum states. Though the initial population of reaction products is distributed over many angular momentum states, the nuclei rapidly de-excite to the states possessing the lowest energy for a given angular momentum (yrast states). The nuclei then de-excite to the ground state via these yrast states with a series of M1 and E2 transitions (the yrast cascade).

The experimental environment of in-beam studies presents several difficulties in observing the isotopes of interest. The isotope samples are observed in a high radiation area which makes very accurate transition energy and intensity determinations difficult. Additionally, several different masses and elements resulting from the reaction may be present in the sources under observation.

By observing the decays of the product nuclei to nuclei of interest many of these problems may be alleviated. The produced parent nuclei that populate levels in the isotope for study decay at rates far slower than the lifetimes of the excited yrast states populated in the (heavy ion, xnγ) reactions. This permits their transport to an

observation environment more conducive to very accurate spectroscopy. More importantly, the produced nuclei may be mass separated, removing considerable ambiguity from the experimental observations. However, decay experiments are statistically and energetically limited to probing the lower levels (below a few MeV) of the nuclear spectra. Many modes of decay from the many populated levels exist and may be observed. This results, in most cases, in a gamma ray spectrum of a few intense transitions accompanied by a myriad number of much weaker lines, many only barely discernible above background. This situation is worsened by the decreasing detection efficiency for high energy transitions. Hence only the lower regions of the spectrum, where states have been fed by transitions from higher levels, can be easily studied.

From the above, it can be seen that in-beam spectroscopy provides a good method for investigating the high energy, large angular momentum states of the nucleus, yet is a poor tool for deducing the detailed structure of the nuclear level scheme outside of the yrast bands. On the other hand, decay studies permit the detailed investigation of this lower energy region and are generally not restricted to bands. Decay studies have the additional advantage of mass-separation capability. Since it is very important to obtain detail on many nuclear states rather than a preferred band of levels, this additional detail provided by decay studies yields a crucial testing ground for nuclear models.

Systematics of the neutron deficient, even-even radon nuclei prior to this study have been very scant. As for the individual isotopes to be studies here, ^{206}Rn and ^{208}Rn, very little detail on the level structures existed. Those studies which had been performed on ^{206}Rn by Inamura et al.,[1] Backe et al.,[2] and Horn et al.,[3] all conflicted

concerning the transition order and lifetimes, as shown in Figure 1; all measurements were made with in-beam spectroscopy. Only one previous study of ^{208}Rn had been performed by Backe et al.[2] with in-beam spectroscopy; the results of this study are shown in Figure 2. Theoretical descriptions of these nuclei[4] were handicapped by this scant amount of information.

These studies represent the first decay studies to be performed on the nuclei ^{206}Rn and ^{208}Rn. The information produced has provided the first systematic picture of their level schemes in detail and has yielded information for interpreting the results of the previous reaction studies.

Additionally, a theoretical approach to the nucleus has been applied in an attempt to understand the underlying structure of these nuclei in some detail, with moderate success. These nuclei are tractable in terms of shell model calculations and such studies are anticipated. This region provided an opportunity, however, to test the applicability of the interacting boson approximation of Iachello and Arima[5-9] to a series of nuclei in this region for the first time. The model has been very successful for nuclei with $Z < 82$ but its application to nuclei above $Z = 82$ has been limited by the paucity of nuclear structure information. It will be seen that the model appears to be a good approach to understanding the features of the observed spectra.

In the process of studying the levels in ^{206}Rn and ^{208}Rn, the experiments undertaken have provided additional detail concerning the alpha decays of the francium parent nuclei, which have been previously studied by several groups. These investigations discovered the existence of an isomer in ^{206}Fr. The alpha decays were studied by a more precise

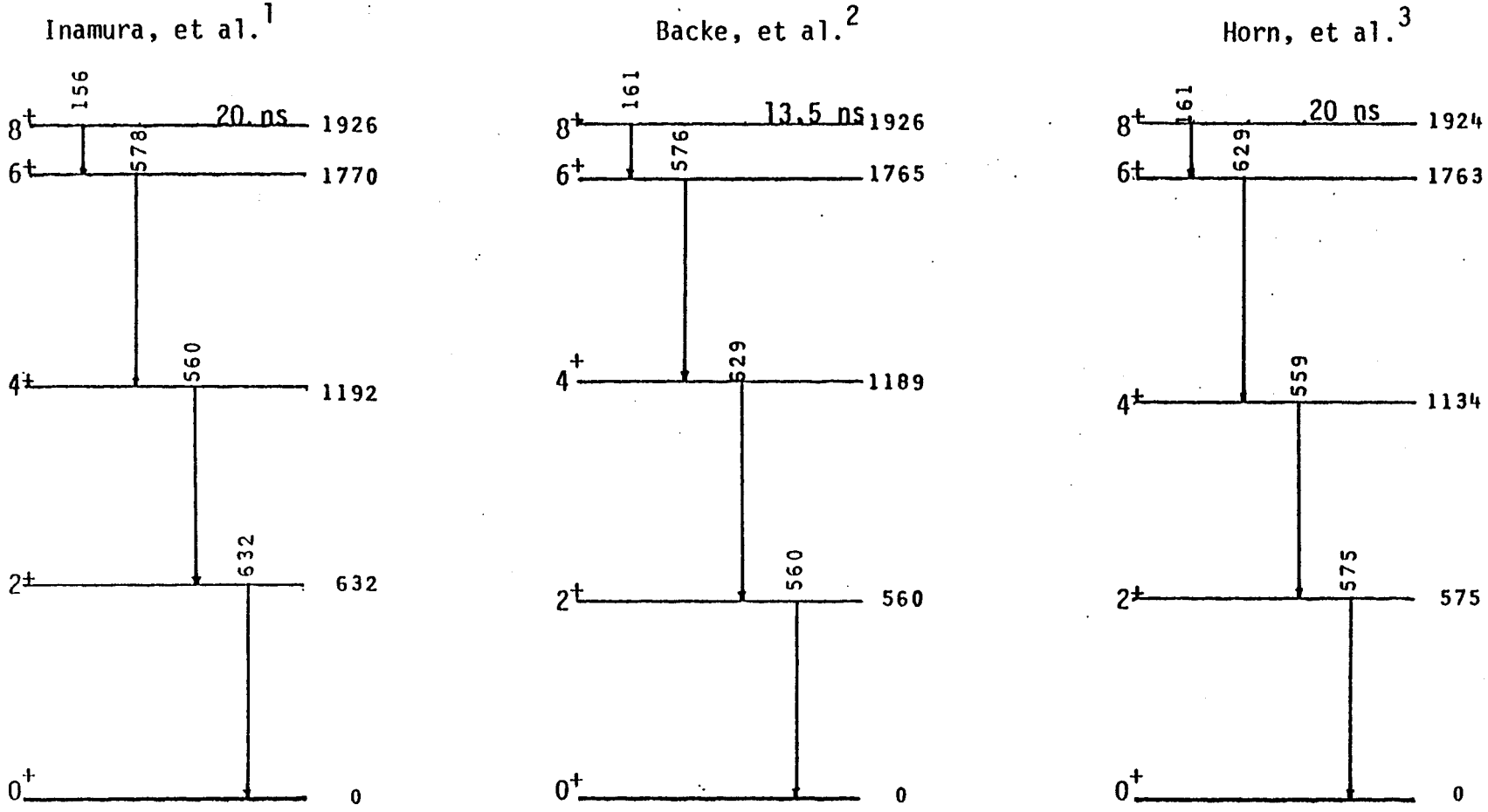

Figure 1. Level schemes for ^{206}Rn proposed prior to this study. Only levels below the 8^+ isomer are shown; considerable disagreement exists above that level.

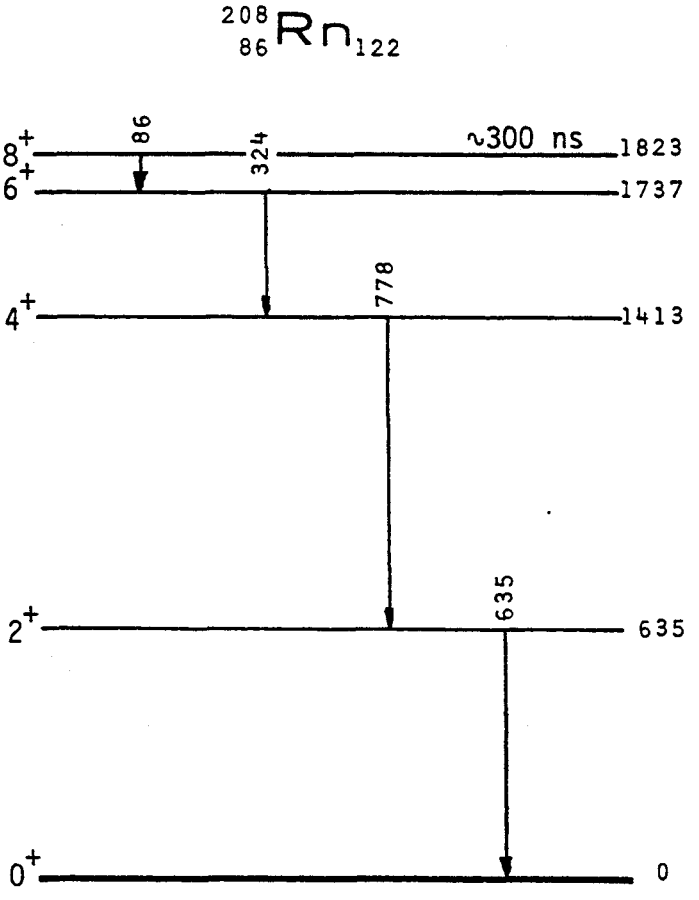

Figure 2. Proposed level scheme for ^{208}Rn by Backe, et al.[2]

method than previously[10,11] used and the new information has been analyzed and correlated with observed systematics of the neutron deficient nuclei above lead.

The theoretical model applied to the radon level schemes is described in the next chapter, followed by a chapter describing the techniques used in these studies. The experimental results for the decays of ^{208}Fr and ^{206}Fr are given in a subsequent chapter, followed by a chapter discussing the interpretation of the results and possible future directions for studies of these and neighboring nuclei.

CHAPTER 2

AN OVERVIEW OF THE INTERACTING BOSON APPROXIMATION OF ARIMA AND IACHELLO

A. Introduction

The general features of the observed even-even nuclear spectra are well known. In particular, heavy even-even nuclei exhibit behavior which mimics collective nuclear motion with but few degrees of freedom. Based on the appearance of the level structures in these cases, these collective spectra are grouped into two broad categories: rotational and vibrational.

In 1952 Bohr and Mottelson proposed a geometrical model[12,13] which possessed limits corresponding to these two cases. This model also incorporated features which went beyond a simple rotor or liquid drop to describe transition probabilities, collective bands within the same nucleus, and other nuclear structure phenomena which until then were less well understood.

Many models have been proposed since which incorporate the features of the geometric description or slightly modify them. These collective models, though more elaborate and successful, in many respects have become less based on the microscopic origins of the nuclear phenomena. All such models appear to be lacking some important feature or features in their Hamiltonians which would make the broad range of observations more coherent and related.

These collective models must overlook much of the physics associated with the nucleus in an attempt to explain the experimental results. It would be tempting to try purely shell model calculations for the nuclei within the transition region. But the sheer immensity of the calculations becomes prohibitive, because commonly matrices arise with orders greater than 1,000,000 to diagonalize.

For a more microscopic picture of the nucleus than that presented by the collective models, there are two alternatives among those available: to develop a shell model truncation scheme which is based on the systematics of more complete calculations, or to exploit different degrees of freedom based on observed nucleon interactions. Neither represents an easy extension from earlier theory.

B. Theory of the Interacting Boson Approximation (IBA)

In all theoretical potentials developed for nuclear interactions, a prime consideration is the incorporation of a pairing correlation. Such an interaction favors the coupling of two identical nucleons to a total angular momentum J of zero. Such an effect causes the ground state of all even-even nuclei to be 0^+ and is the dominant feature of the nuclear force.

The presence of this J = 0 coupling prompts an attempt to explain nuclear spectra utilizing this as the predominant feature of a theoretical model. Such a model is the Bardeen-Cooper-Schrieffer, or BCS model of nuclear structure,[14] based on the initial application of that theory to the phenomonon of superconductivity.[15] The BCS potential pairs time-reversed states and may be written in second quantitized

form as

$$H = -G \sum_{kk'} a_k^+ a_{k'}^+ a_k a_{k'} \quad . \tag{2.1}$$

Though useful in explaining the character of some states in even-even nuclei and other nuclear phenomena, it has not been very productive in providing any detailed nuclear level schemes. From this failure it would appear that other dynamical variables (degrees of freedom) are needed.

A logical extension of the BCS model is to incorporate other multi-nucleon couplings. In Figure 3, the two-identical-nucleon couplings for all the levels through the f-p-g shell of the shell model are shown, plotted with respect to spin and energy. The interaction used is the Hamada-Johnson potential, and the calculated matrix elements are those of Kuo and Brown.[16,17] It appears that couplings with J as high as 4 could be useful to consider in an extension of the BCS approach, but those with J equal to or higher than that probably represent unlikely ($E > 0$) pairs and are probably not prevalent in low-lying spectra at all.

When coupling identical nucleons, the coupled pair has isotopic spin 1, a quantity believed to be conserved in nuclear interactions based on experimental evidence (i.e.: isospin families in nuclear spectra). Such a conservation rule reduces the number of nucleon couplings which need to be considered. For a properly antisymmetrized, coupled identical nucleon system, only even L couplings need to be considered for inclusion in the degrees of freedom.

The next extension, then, from the $L = 0$ model would be to include $L = 2$ couplings. The model Hamiltonian would be made up of terms which

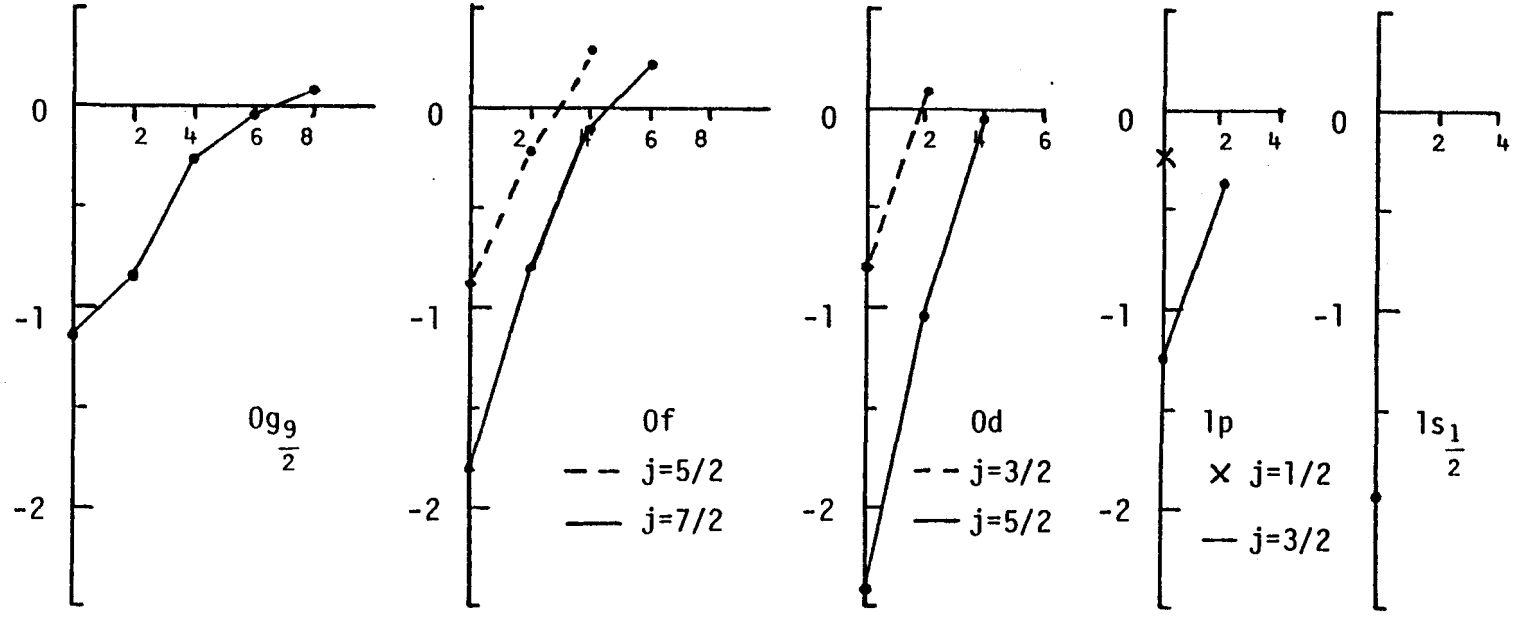

Figure 3. Matrix elements for T = 1 two nucleon couplings (Kuo and Brown, references 16 and 17). Vertical axes denote energy (in MeV); horizontal axes denote coupled angular momentum (in units of $\hbar$). Shell designations are at the lower right of each figure.

couple nucleon pairs together with different configuration J values. It is from this concept that Iachello and Arima developed the interacting boson approximation for even-even nuclei.[5-9]

In developing their model the following terminology was adopted: The coupled pairs of fermions are referred to as "bosons" since the pairs have integral spin. The L = 0 pairs are referred to as s-bosons and the L = 2 couplings as d-bosons. Further, the number of bosons is constrained by the number of valence nucleons. Here the valence nucleons are those particles or holes which are added to the nearest closed shell core (i.e.: ^{40}Ca, ^{132}Sn, ^{208}Pb). The core is assumed to be inert. Core inertness is a reasonable assumption because of the large nuclear shell gap at magic numbers, and such an approximation is typically used for the most complete shell model calculations. The number of bosons is given by half the total number of valence nucleons.

At this point it is important to note several links to the underlying shell model. The nucleon couplings are those which could be predicted microscopically in shell model calculations. The number of bosons used is specifically constrained to be half of the number of interacting nucleons in the nucleus, with the core considered inert. Finally, the identical j-shell nature of the boson constituents limits the couplings available to L = 0 and L = 2, to a first approximation.

The system developed thus far consists of two types of "particles" which are called bosons. The interaction between these bosons may be difficult or impossible to establish microscopically. The situation is analogous to the elementary particle strong interaction problem, in that the exact nature of the interaction is unknown. Instead of attempting to explicitly construct a model Hamiltonian from physical observations,

the approach used there is of a group theoretical nature exploiting the symmetries involved.

In the same manner, Arima and Iachello developed a model Hamiltonian based on the symmetries involved in a boson description like that described above. Their approach differs from the boson models of other theorists by exploiting these symmetries. With this approach it becomes possible to postulate unbroken boson symmetries as limiting cases and to develop simple analytical formulae for facilitating comparison with experimental results.

Using the s- and d-bosons, their six components span six dimentional space and provide a linear basis for an SU(6) group representation. With these N bosons, the only allowed representations are those which are totally symmetric with respect to the interchange of any two bosons; these are chosen from a partition (N) of SU(6). In the absence of a residual interaction or d-s energy difference ($\varepsilon_d - \varepsilon_s$), the energy levels are all degenerate. With a residual interaction and a d-s energy difference, the general Hamiltonian is

$$
\begin{aligned}
H = {} & \varepsilon_s s^+ s + \varepsilon_d \sum_m d^+ d \\
& + \sum_{J=0,2,4} \frac{1}{2} \sqrt{2J+1} \; \langle d^2 J | V | d^2 J \rangle \; [(d^+ d)^{(J)} \; (dd)^{(J)}]^{(0)} \\
& + \langle ds2 | V | d^2 2 \rangle \; [(d^+ d^+)^{(2)} \; (ds)^{(2)} + (d^+ s^+)^{(2)} \; (ds)^{(2)}]^{(0)} \\
& + \langle d^2 0 | V | s^2 0 \rangle \; [(s^+ s^+)^{(0)} \; (dd)^{(0)} + (d^+ d^+)^{(0)} \; (ss)^{(0)}]^{(0)} \\
& + \langle ds2 | V | ds2 \rangle \; [(d^+ s^+)^{(2)} \; (ds)^{(2)}]^{(0)} \\
& + \langle s^2 0 | V | s^2 0 \rangle \; [(s^+ s^+)(ss)] \qquad (2.2)
\end{aligned}
$$

The quantum numbers within the bras and kets denote the boson configurations of the states and their angular momentum. The numbers enclosed within the parentheses as superscripts denote angular momentum couplings.

It is seen that H has nine parameters in all: ε_s, ε_d, and the two-body interaction matrix elements. After choosing these nine parameters, the Hamiltonian may be diagonalized between states with various numbers of bosons and values of total angular momentum, subject to the number constraint on the bosons described earlier. The matrices will be of reasonable size for computation (typically on the order of N).

It is possible to consider limiting cases which give analytical formulae for the energy of the levels. These formulae make comparison between the experimental results and IBA predictions very easy. These limits are found by assuming different relative magnitudes for the various boson couplings. An equivalent way of arriving at the same limit is to assume some form of the Hamiltonian, and then derive a set of parameters for equation 2.2 which render it in the same form as the assumed Hamiltonian. This approach will be illustrated below.

With respect to group theory, what is intended is to show that the Hamiltonian may be written in terms of the generators of SU(6). The 35 generators G_i may be decomposed to exhibit other symmetries, since SU(6) has as subgroups H_i many lower dimension symmetry groups, say of dimension P. Thus, if we find a Hamiltonian invariant under the P dimensional orthogonal group (with $P < 6$) for instance, the initial SU(6) Lie algebra will contain the O(P) Lie algebra and reproduce it with a suitable choice of parameters. We have, then, performed the decomposition

$$SU(6) \rightarrow O(P) \ .$$

The states of the O(P) representation may be labeled by the variables used to identify the various representations within the two groups, SU(6) and O(P).

For the group SU(6), there are but three possible decompositions:

$SU(6) \rightarrow SU(5)*U(1)$

$SU(6) \rightarrow SU(3)*SU(2)$

$SU(6) \rightarrow O(6) \rightarrow O(5) \rightarrow O(3)$.

The Hamiltonian of equation 2.2 accordingly has three dynamical symmetries based on these decompositions. The invariant form of the Hamiltonian possesses operators which commute with the orthogonal transformations of the particular group structure. The eigenstates would be those vectors invariant under the same set of transformations. The states can be labeled by the variables used to denote the various representations of the groups in the decomposition.

The IBA has been the subject of much theoretical nuclear research in the past several years, and possesses extensive literature. The seminal papers[5-9] by Iachello, Arima, and co-workers remain the best thorough introductory works on the theory in all its aspects. In the next sections, those aspects of the theory pertinent to this study are discussed briefly. Further detail may be obtained from the references cited in the section headings.

All of the following figures in this chapter are taken from reference 18.

C. Symmetries of the IBA Hamiltonian

1. Vibrational Spectra[5]: SU(5)

If the s-boson degree of freedom is of small importance in the

Hamiltonian of equation 2.2, the Hamiltonian may be simplified to the form:

$$H = \varepsilon_d \sum_m d^+ d + \sum_{J=0,2,4} \frac{1}{2}\sqrt{2J+1}\, \langle d^2 J|V|d^2 J\rangle\, [(d^+ d^+)^{(J)}(dd)^{(J)}]^{(0)}. \quad (2.2b)$$

The terms $\langle d^2 J|V|d^2 J\rangle$ for J = 0,2,4 may be denoted as c_0, c_2 and c_4, respectively.

Equation 2.2b is a Hamiltonian which essentially has two levels. The additional term of the summation splits the degenerate upper level into J = 0, 2, and 4 levels. Such a spectrum as a basis strongly suggests a vibrational nucleus in the Bohr-Mottelson scheme. This limit, since it considers only the d boson degrees of freedom, is sometimes called the d-boson limit.

The 5 magnetic substate components of the d level form a linear basis for an SU(5) group representation. To uniquely specify states in this space, 5 quantum numbers are needed. With boson conserved, n_d is a good quantum number as well as J and M.

The two remaining quantum numbers are chosen to describe how the boson configurations are made up, based on seniority. Seniority v denotes the number of bosons remaining after the L = 0 coupled pairs are removed from the configuration. (Sometimes, instead of the seniority v, the number n_β of boson pairs coupled to zero total angular momentum is considered. The relationship between seniority v and n_β is simply $v = n_d - 2n_\beta$.) Finally, a fifth quantum number n_Δ counts the number of boson triplets coupled to L = 0.

The total energy spectrum can then be given by

$$E(n_d,v,n_\Delta,J,M) = \varepsilon_d n_d + \frac{\alpha}{2} n_d (n_d - 1)$$

$$+ \beta(n_d - v)(n_d + v + 3)$$

$$+ \gamma[J(J - 1) - 6n_d] \quad . \qquad (2.3)$$

The relationship between equation 2.3 and the d-boson limit Hamiltonian given in equation 2.2b may be seen by letting n = 2, with J = 0, 2, or 4. For $n_d = 2$, J = 0 (i.e., v = 0), 2.3 reduces to

$E = 2\varepsilon_d + \alpha + 10\beta - 12\gamma$.

Equation 2.2b for this case gives

$E = 2\varepsilon_d + c_0 \rightarrow c_0 = \alpha + 10\beta - 12\gamma$.

Similarly it is possible to show that

$c_2 = \alpha - 6\gamma$ and $c_4 = \alpha + 8\gamma$.

A typical spectrum is shown in Figure 4(a) for equation 2.3. The bands developed are characterized by multiplets based on n, such that the available J values for the maximum seniority states are $2n_d$, $2n_d - 2$, $2n_d - 3$, . . . n_d.

The additional bands, formed by configurations with less than maximum seniority are shown to the right of the figure in separate bands. The band notation is that used by Iachello and Arima.

The similarities between the spectra of this limit of the IBA and the vibrational spectra of the Bohr-Mottelson description are evident. Particularly noticeable are the uniform spacings of the multiplets, characterized by the energy of the first excited state, and the "two phonon" triplet--4^+, 2^+, 0^+--at roughly twice the energy of the first excited state. In fact, the SU(5) limit proves to be very successful in describing the so-called vibrational nuclear spectra.

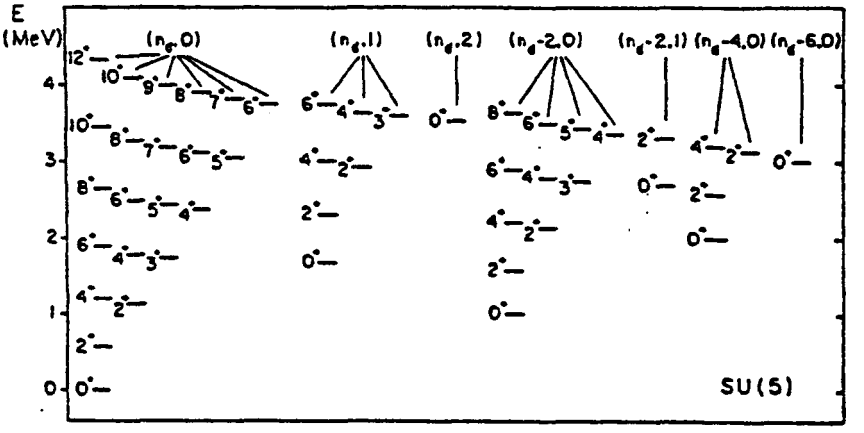

(a)

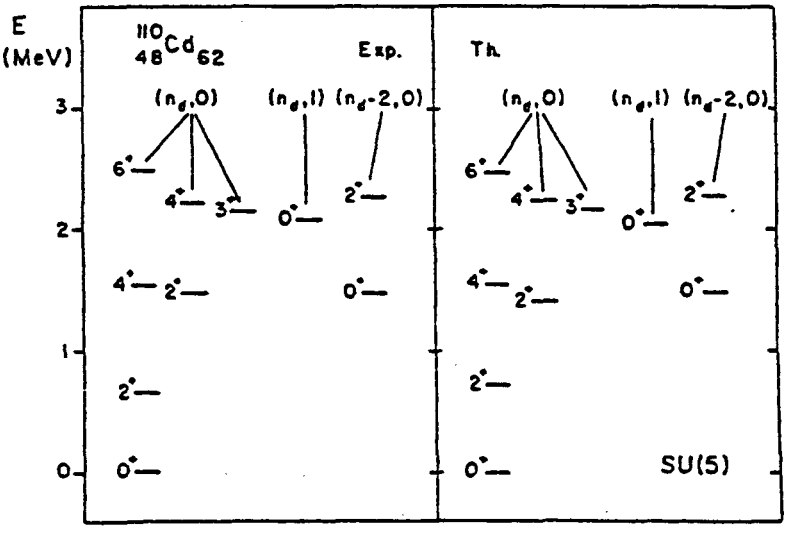

(b)

Figure 4. Theoretical and experimental spectra exhibiting SU(5) symmetry in the IBA. (a) A typical spectrum with N = 6. In parenthesis are the values of v and n_Δ. (b) An experimental spectrum with SU(5) symmetry: ^{110}Cd, $^{\Delta}$ (N = 7). The theoretical energies are calculated using (2.2) with ε = 722 keV, α = 18 keV, β = 10.3 keV, γ = 10 keV. (from reference 18)

An example, ^{110}Cd, is shown in Figure 4(b). All observed experimental levels are predicted by the IBA. The energy levels and spacings are accurately given by the analytical formula, and the agreement is impressive.

2. Rotational Spectra[6]: SU(3)

In the SU(5) limit, several terms of the full Hamiltonian of equation 2.2 were assumed to be insignificant. This may not always be the case; there are still two possible symmetries remaining in the full Hamiltonian, however, and attention is turned to them now.

The use of SU(3) symmetry considerations in the study of nuclear spectra was treated in 1958 by Elliot[19] with a quadrupole-quadrupole interaction only. It was found to be a moderately successful tool in explaining some of the features of s-d shell nuclei, notably ^{20}Ne and ^{24}Mg.

Since the IBA incorporates s- and d-bosons, it would seem possible that an SU(3) limiting case of the Hamiltonian in equation 2.2 could be useful in furthering the understanding of nuclear physics. The Hamiltonian is similar to that of Elliott with an additional j-j interaction included. The SU(3) Hamiltonian, where the Q and J are the quadrupole moments and angular momenta, is

$$H = -\kappa \sum_{ij} Q_i \cdot Q_j - \kappa' \sum_{i,j} J_i \cdot J_j \quad . \tag{2.4}$$

Equation 2.4 has two separate terms, the sum of which is known to exhibit SU(3) symmetry. The quadrupole-quadrupole interaction may be expressed in second quantitized form[6] as

$$Q^{(2)} = \sum_{m} (d^{+}s + s^{+}d)^{(2)}_{m} - \frac{7}{2} (d^{+}d)^{(2)}_{m} \tag{2.5a}$$

while the $J_i \cdot J_j$ term may be written as

$$J^{(i)} = \sum_m \sqrt{10} \quad (d^+d)^{(i)}_m. \qquad (2\text{-}5b)$$

There are five terms in Q and three terms in J; the components are actually all the generators of SU(3), and there are $(3^2 - 1) = 8$ of them. Indeed, if an initial symmetry group of U(6) is considered, we notice that equations 2.5 represent a subset of the 36 generators for that higher symmetry:

$$(s^+s),\ (d^+s)^{(2)}_m,\ (s^+d)^{(2)}_m,\ (d^+d)^{(0)}_m,\ (d^+d)^{(1)}_m,\ (d^+d)^{(2)}_m,$$
$$(d^+d)^{(3)}_m, \text{ and } (d^+d)^{(4)}_m$$

constituting 36 operators in all. The operators of equation 2.5 form a proper subset of U(6), and therefore it should be possible to cast that equation in the form of equation 2.2 with a suitable choice of parameters, as is the case for the SU(5) limit.

The choice of parameters given in Table 1 renders equation 2.2 equivalent to equation 2.4. The decomposition used in SU(6) → SU(3) → O(3) in equations 2.5. The states can be labeled in terms of: (N), the partition of SU(6) used; the irreducible representation of SU(3) used, usually given by (λ,μ), after Elliott[19]; and the quantum numbers of O(2), J and its projection along some axis.

The quadrupole-quadrupole interaction can be written explicitly in terms of J and the Casimir operator for the SU(3) group[20] as

$$\kappa Q \cdot Q = -\kappa[C(\lambda,\mu) - \tfrac{3}{4} J(J + 1)]$$

where

$$C(\lambda,\mu) = \lambda^2 + \mu^2 + \lambda\mu + 3(\lambda + \mu).$$

Table 1. Values of the Coefficients ε_s, ε_d, c_L, v_L, u_L which Correspond to the Q·Q and L·L Boson Interaction. (from reference 6)

Parameter	Form in 2.2	$-4Q\cdot Q$	$L\cdot L$
ε_s	ε_s	-20	0
ε_d	ε_d	-11	6
c_0	$\langle d^2 0 \vert V \vert d^2 0\rangle$	-14	-12
c_2	$\langle d^2 2 \vert V \vert d^2 2\rangle$	3	- 6
c_4	$\langle d^2 4 \vert V \vert d^2 4\rangle$	- 4	8
v_2	$\langle ds2 \vert V \vert ds2\rangle$	$4\sqrt{70}$	0
v_0	$\langle d^2 0 \vert V \vert d^2 0\rangle$	$-8\sqrt{5}$	0
u_2	$\langle ds2 \vert V \vert ds2\rangle$	$-8\sqrt{5}$	0
u_0	$\langle s^2 0 \vert V \vert s^2 0\rangle$	0	0

With this equation, the initial Hamiltonian for SU(3) symmetry may be written as

$$E\ ([N],\ (\lambda,\mu),\ \chi,\ J,\ M) = \alpha\ J(J+1) + \beta\ C(\lambda,\mu) \qquad (2.6)$$

where χ is an additional quantum number used to differentiate between those states with the same (λ,μ) and J. Here

$$\alpha = \frac{3}{4}\kappa - \kappa' \text{ and } \beta = \kappa.$$

The spectrum generated by equation 2.6 is shown in Figure 5(a). The various representations (λ,μ) give rise to rotational bands. Levels within these bands are strongly connected by electromagnetic transitions[6]. In the limit $N \to \infty$, the spectrum becomes that of the Bohr-Mottelson rotational description, which may be written as

$$E_{BM} = \alpha\ J(J+1) + \beta n_\beta + \gamma n_\gamma$$

where n_β and n_γ are the quanta of vibration for the β and γ bands of the geometric Hamiltonian. Such a spectrum is observed for many nuclei around the midpoint between closed shells. One such example, compared with the results of equation 2.6, is shown in Figure 5(b), in this case ^{156}Gd. Again, excellent agreement between theory and experiment is found without resorting to the full Hamiltonian of equation 2.2. All observed states are predicted by the theory.

In this section it has been seen that the original IBA Hamiltonian of equation 2.2 may be recast into a form which exhibits SU(3) symmetry by a suitable choice of parameters. The eigenvalue problem then becomes equivalent mathematically to that studied by Elliott with the inclusion of a J-J term.

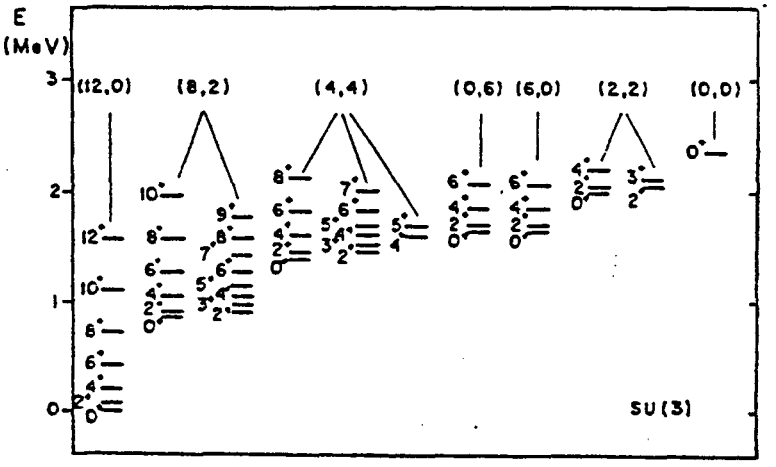

(a)

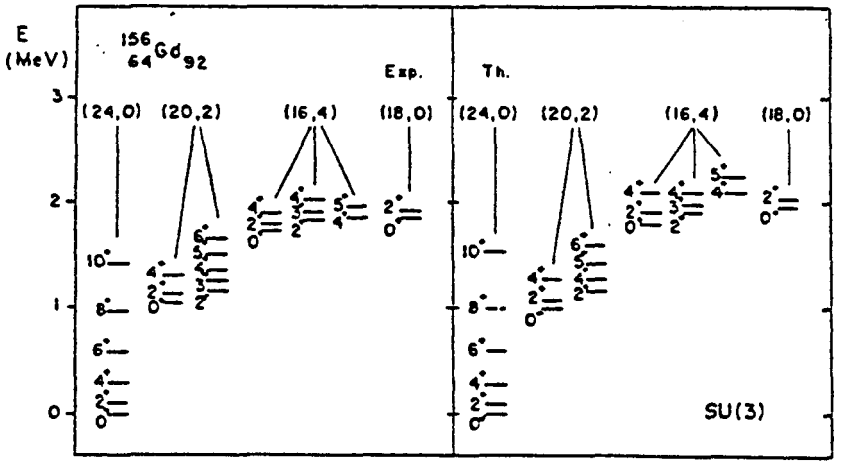

(b)

Figure 5. Theoretical and experimental spectra exhibiting SU(3) symmetry in the IBA. (a) A typical spectrum with N = 6. In parenthesis are the values of λ and μ which label the SU(3) representations. (b) An experimental spectrum with SU(3) symmetry: ^{156}Gd, (N = 12). The theoretical spectrum is calculated using (2.3) with κ = 7.25 keV, κ' = 8.56 keV. (from reference 18)

3. Triaxial rotor-like spectra; O(6)[9].

The remaining symmetry of equation 2.2 has been found to be useful in the IBA approach to nuclear spectra. This limit uses the following decomposition of the Hamiltonian:

$$SU(6) \rightarrow O(6) \rightarrow O(5) \rightarrow O(3).$$

In such a scheme, states may be labeled by: σ, denoting the O(6) irreducible representation; τ, corresponding to the O(5) irreducible representation; and J and M, which label the O(3) representation. An additional quantum number, n_Δ, is also used, but has no effect on the energy eigenvalues. An analytic formula will yield an expression for the energies in terms of these labels for each partition (N) of SU(6) for N bosons.

The Hamiltonian for the decomposition may be written[20]

$$H = aG_6 + bC_5 + cC_3, \tag{2.7}$$

where G_6 is the pairing operator of O(6), C_5 is the Casimir operator of O(5), and C_3 is the Casimir operator of O(3). In an O(6) vector basis, the Hamiltonian of equation 2.7 has O(6) symmetry.

For the pairing operator G_6,

$$\langle G_6 \rangle = \frac{1}{4} (N - \sigma) (N + \sigma + 4).$$

The Casimir operators for O(5) and O(3) are $\tau(\tau + 3)$ and $J(J + 1)$, respectively, in representations diagonal in τ and J. Hence, equation 2.7 has energy eigenvalues

$$E(N,\sigma,\tau,n_\Delta,J,M) = \frac{a}{4} (N - \sigma)(N + \sigma + 4) + b\tau(\tau + 3) + c\, J(J + 1) \tag{2.8}$$

A spectrum generated by this equation is shown in Figure 6(a). An

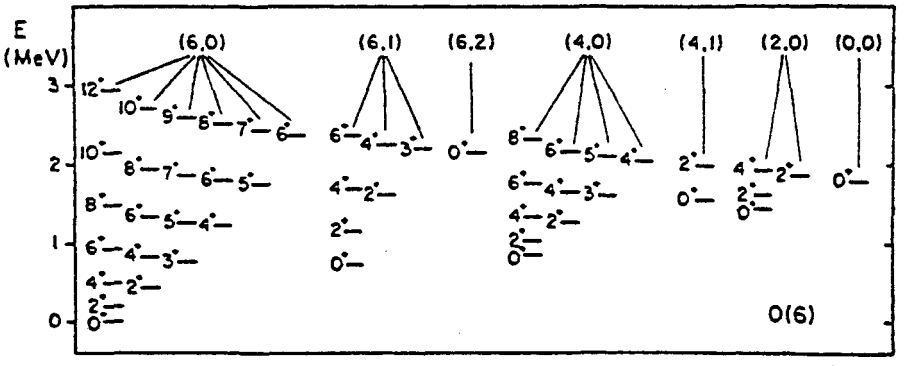

(a)

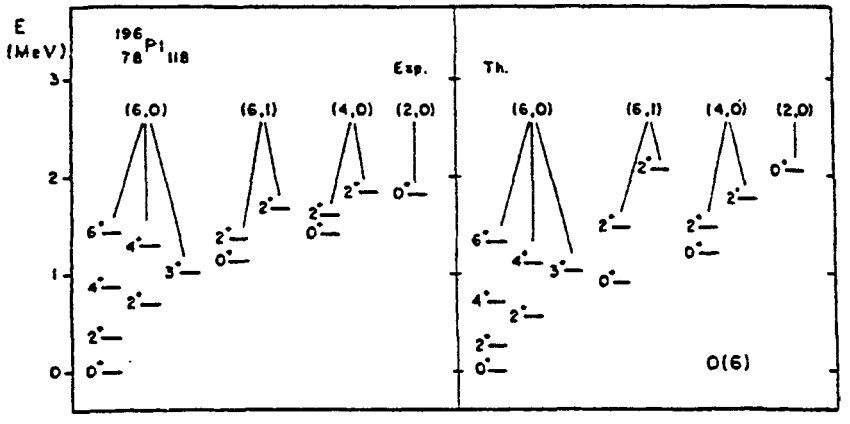

(b)

Figure 6. Theoretical and experimental spectra exhibiting O(6) symmetry in the IBA. (a) A typical spectrum with O(6) symmetry and N = 6. In parenthesis are the values of σ and ν_Δ. (b) An experimental spectrum with O(6) symmetry: ^{196}Pt, (N = 6). The theoretical spectrum is calculated using (2.4) with A = 172 keV, B = 50 keV, C = 10 keV. (from reference 18)

example of this symmetry appears in Figure 6(b), in this case ^{196}Pt. Excellent agreement between theory and experiment is seen, though the example shown does not exhibit as good an agreement between theory and experiment as was seen with the previous two limits. The spectrum is seen to consist of near identical multiplets with the upper levels in the preceding multiplet absent. The spectrum of Figure 6(b) is similar to that of a completely soft vibrator of Wilets and Jean[21], or a triaxial rotor.

D. Electromagnetic Transitions

The previous part of this chapter dealt briefly on the three limits of the IBA, primarily to illustrate the energy spectra of those limits. A sensitive test of the theoretical predictions of nuclear models is the calculation of electromagnetic transition matrix elements. These predictions, which may be verified directly by experiment, are crucial indicators of the validity of the assumption made in constructing the model Hamiltonian.

If only bilinear products of boson operators are considered in constructing a general electromagnetic transition operator, that operator $T_q^{(k)}$ may be written[5]

$$T_q^{(k)} = \alpha_k \, (d^+ s + s^+ d)_q^2 \; \delta_{k2} + \beta_k \, (d^+ d)_q^k + \gamma_k \delta_{k0} \, (s^+ s)_0^{(0)} \qquad (2.9)$$

Only transitions which do not change parity are described by this operator since all states predicted by the s-d boson model have positive parity.

The most commonly observed transitions in even-even nuclei are the M1 and E2 multipolarities. Equation 2.9 for those operators gives

$$T(M1) = \sum_m \beta_1 \, (d^+ d)_m^1 \qquad (2.10)$$

and

$$T(E2) = \sum_m \alpha_2 \, (d^+s + s^+d)^2_m + \beta_2 \, (d^+d)^2_m. \qquad (2.11)$$

The M1 operator is diagonal in a model based on states where the number of d bosons is a good quantum number. The IBA, then, predicts no M1 transitions if the operator of equation 2.9 is restricted to bilinear products. It can be shown that[5], when extended to higher orders, the general transition operator gives rise to M1 transitions.

The E2 operator of equation 2.11 can give rise to transitions between different multiplets and within the multiplets. However, equation 2.11 cannot change n_d by 2 or more, nor change the angular momentum by more than 2. These may be expressed succinctly in the selection rule.

$$|\Delta n_d| \leq 2 \text{ with } |\Delta J| \leq 2 \qquad (2.12)$$

It can be shown[5] that as the nucleus goes to higher angular momentum, the transitions between multiplets become very weak. This yields a band structure within the nucleus, where series of levels are connected in cascade by E2 transitions.

Iachello and Arima have analyzed several series of even-even isotopes to compare the calculated and experimental reduced matrix elements for these transitions[20]. The agreement between experiment and theory is strong, as shown in Figure 7. Such analyses are handicapped at this time due to the scarcity of measured B(E2) values for series of isotopes. However, for those series for which detailed B(E2) measurements exist, the agreement between observed and calculated values is strong and provides convincing proof for the model.

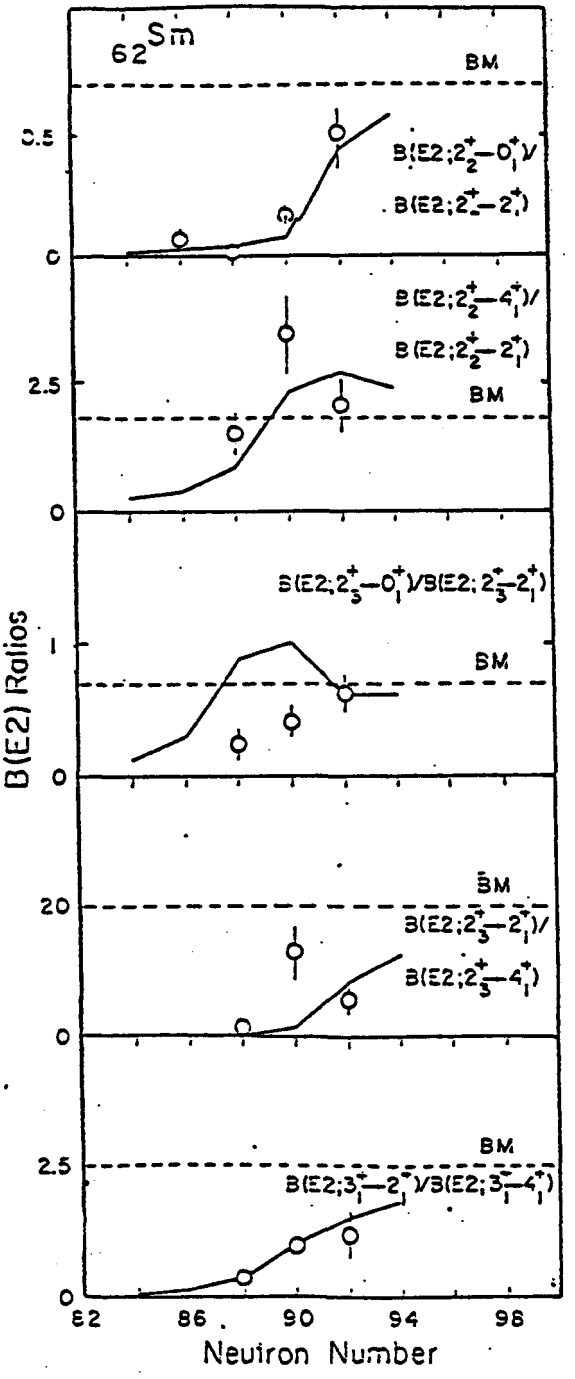

Figure 7. Theoretical and experimental (circles) B(E2) ratios for samarium isotopes (from reference 7).

E. Extensions of the Model

Several additional items are discussed briefly here to outline extensions and enhancements of the model which exist or are under development.

In addition to the s- and d-bosons, one might consider additional degrees of freedom. Figure 3 could be extended to justify a third degree of freedom, a J^{π} = 3- or f-boson. Such a boson would introduce negative parity states into a spectrum with its interactions with the other bosons. This octupole excitation has been thoroughly investigated[5-9]. With such an excitation included, transition operators which change parity as well as angular momentum can be discussed within the framework of the model. Many of the predictions of this extension of the s-d boson model are in agreement with experiment[18].

Extending the model to odd-A nuclei[22] has proceeded along the lines of most particle-plus-core models. The theory currently presents a limited tool for investigation of these nuclei, and, due to its very recent development, its correspondence with experiment has not been investigated to any great extent.

Much of the ongoing development at this time is directed toward establishing the boson-boson interaction more exactly, mainly with respect to the effects of the boson constituents on the interaction. A neutron-proton IBA theory exists[23] but has not been applied to experimental data to any great extent. The microscopic construction of the bosons is attracting attention[24-27], along with other theories based on bosons[28-30].

In summary, the interacting boson approximation represents a developing theory that has achieved moderate success at an early stage of development. Since its predictions can be checked against experiment

quite easily, a great deal of experimental nuclear physics data are being scrutinized with the IBA. Its application to the region $50 < Z < 82$ has been quite extensive and illuminating. The extension of the model to other regions of the chart of the nuclides has been limited, and experimental efforts are being directed into those areas, of which this work is one.

CHAPTER 3

PRODUCTION OF ISOTOPES FOR STUDY, DATA ACQUISITION, AND DATA ANALYSIS

A. Production of Heavy-Ion Beams at ORIC

The heavy-ion beams were generated by the Oak Ridge Isochronous Cyclotron (ORIC). The reaction used was

$$\text{natural}_{Ir}(^{20}Ne^{5+}, xn)\ ^{206,\ 208}Fr$$

at beam energies of 113 to 125 MeV on target. This energy range was selected by using the liquid drop fission code ALICE[31]. In general, the cyclotron was adjusted to provide the highest energy available and, suitable degrader foils were introduced into the beams near or on the target. Beam currents during the run averaged about 200 particle-nanoamperes (one microampere) during the course of the experiments.

Several experiments were made for this study, and the various beam energies, experiment durations, ion sources and targets used, and measurements made are summarized in Table 2. The projectile beam was delivered to the UNISOR facility via a permanent beam line and associated optics from ORIC, as shown in Figure 8. The figure also shows the other experimental facilities at the Holifield Heavy Ion Research Facility (HHIRF), including the location of the 25 MeV tandem accelerator under construction. A system of cabling interconnects the various experimental areas and the control room. The cabling network also permitted data

Table 2. Summary of experiments which formed the basis of these studies. All targets used were 2-5 mg/cm^2 natural iridium impregnated on graphite felt. All coincidence measurements included simultaneous multiscaling of radiations.

Date begun	Duration of experiment	Neon beam energy†	Ion source used	Measurements made during experiments
31 Aug 78	8 hr	113 MeV	SIS	α, γ multiscale (A=206-208)
15 Sep 78	16	111	HTIS	e^-, γ multiscale, γ-γ-t (A=208)
6 Mar 79	48	119	HTIS	α, γ multiscale (A=204) α, γ multiscale, γ-γ-t (A=206)
14 Jun 79	30	122	HTIS	α, γ multiscale (A=205-208) γ-γ-t (A=206, 208)
2 Aug 79	48	120	HTIS	α, γ multiscale (A=205,206,208) γ-γ-t (A=206) γ-e^--t (A=206,208) accurate energy procedure¶

† Beam energy on target.

¶ Procedure to determine alpha and gamma energies to high accuracy. See discussion in section F of this chapter.

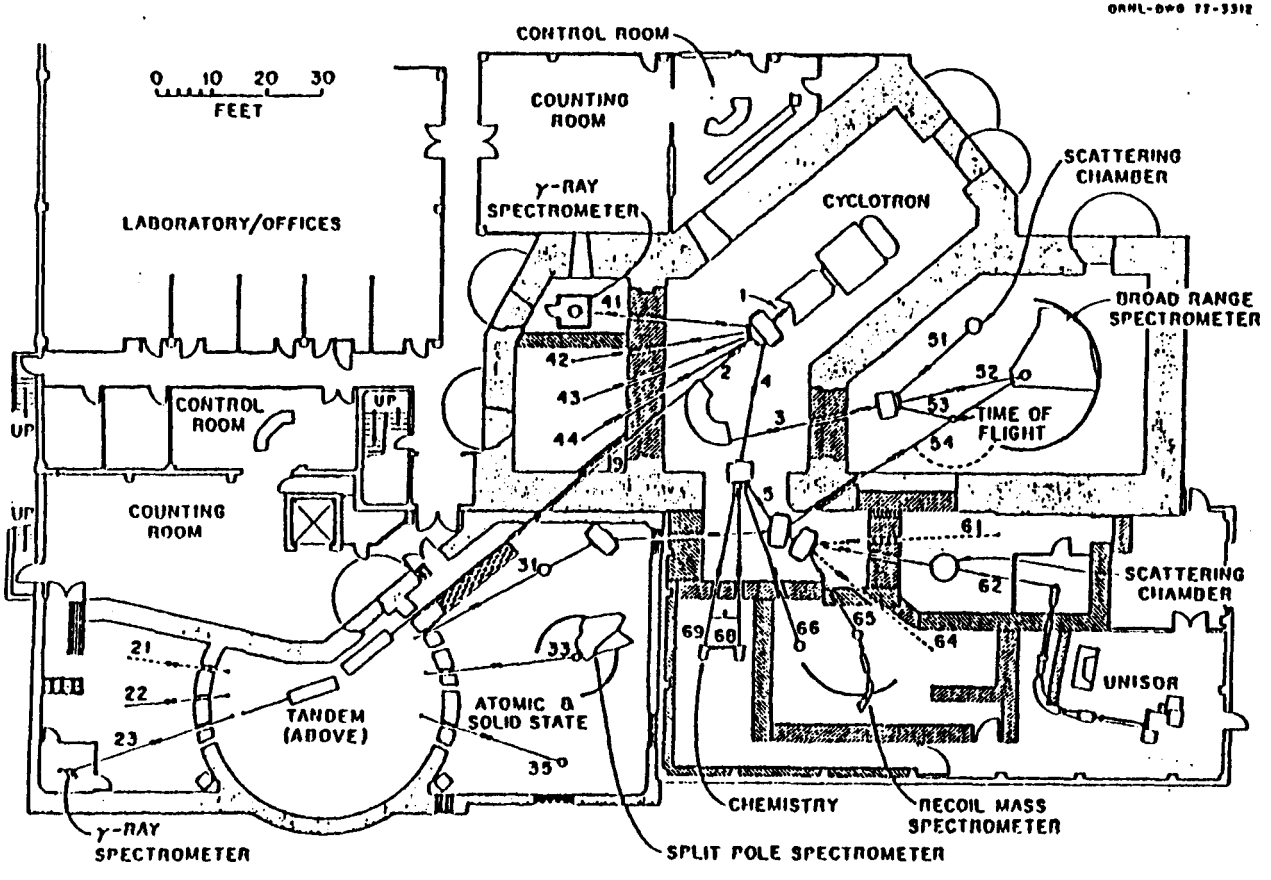

Figure 8. The layout of the experimental floor of the Holifield Heavy Ion Research Facility showing the location of ORIC and UNISOR. Some of the areas shown are under development. The numbers on the figure denote beam line number designations.

transfer to either of two SEL 840A computers located in the ORIC building.

Beam intensity monitoring was principally accomplished by mechanically introducing a beam stop into the beam and measuring the deposited current. Additional optimizing of the beam profile and position was sometimes performed by minimizing the current measured on a series of aligned collimators near the target.

B. Isotope Production and Mass Separation

As mentioned above, ALICE calculations were made for the reaction selected to optimize the production of francium by considering the total production cross-section. The results of these calculations are shown in Figure 9. These cross-sections may best represent lower limits, since copious amounts of ^{208}Fr were produced at all of the energies used, in amounts far greater than for any other mass, contrary to what might be expected from Figure 9. Most of the cross-sections for masses 205-208 are greater than 2 millibarns at the energies used. With approximately 200 particle-nanoamperes of heavy ion beam on target the isotope production for these masses was on the order of 10^4 to 10^5 nuclei per second at target, and roughly a power of ten lower at deposition.

Once produced, the francium atoms were ionized by surface ionization using one of two ion sources being developed by E. H. Spejewski, R. L. Mlekodaj, and the author. The descriptive names for these ion sources are the surface-ionization ion source (abbreviated SIS) and the plasma high temperature ion source (abbreviated HTIS).

The SIS shown in Figure 10 is basically identical to the version used in the experiment of August, 1978. In the ion source reaction pro-

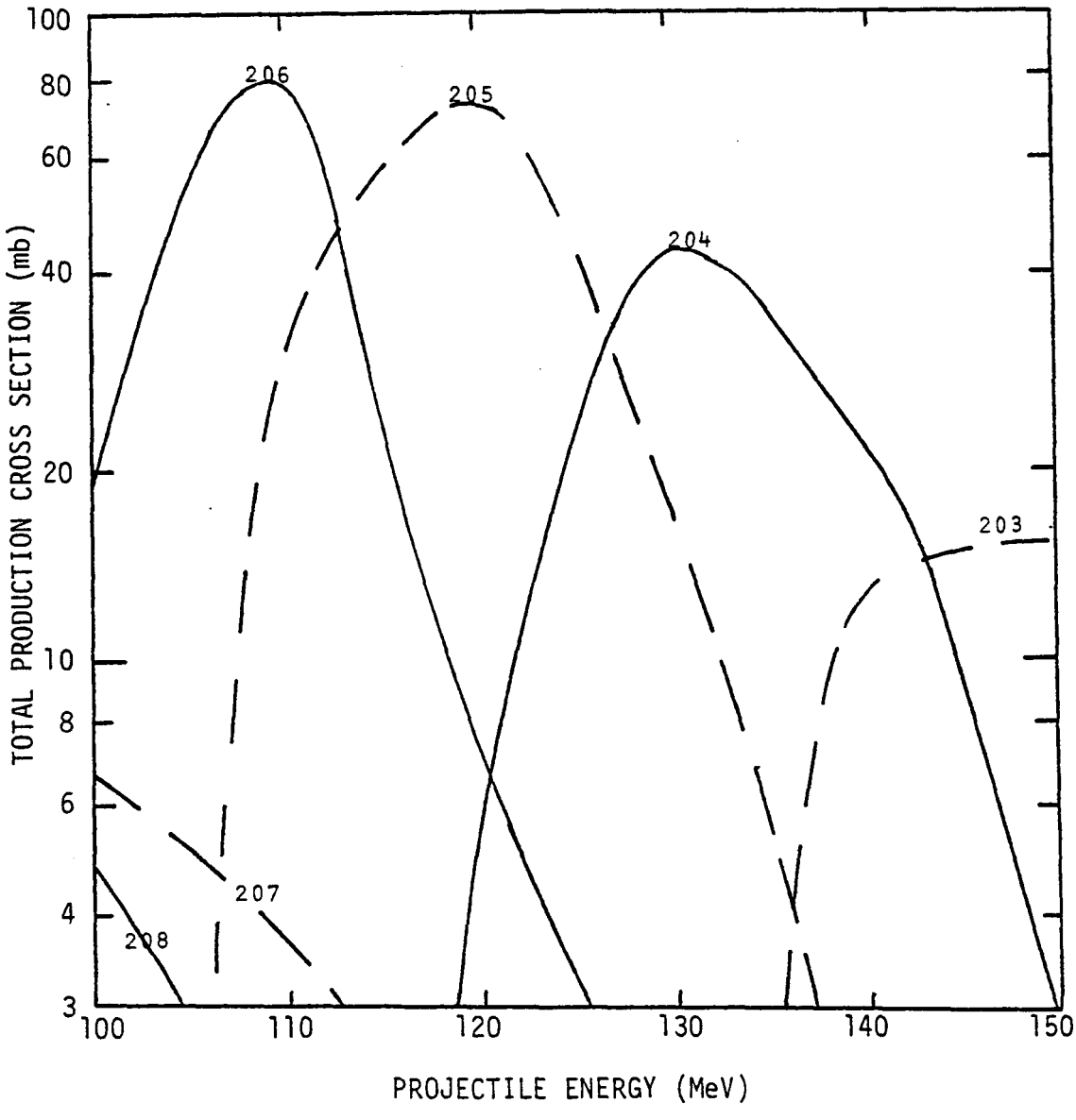

Figure 9. ALICE calculations for ^{20}Ne incident on natural iridium. The numbers on the curves denote the mass numbers of produced francium nuclei.

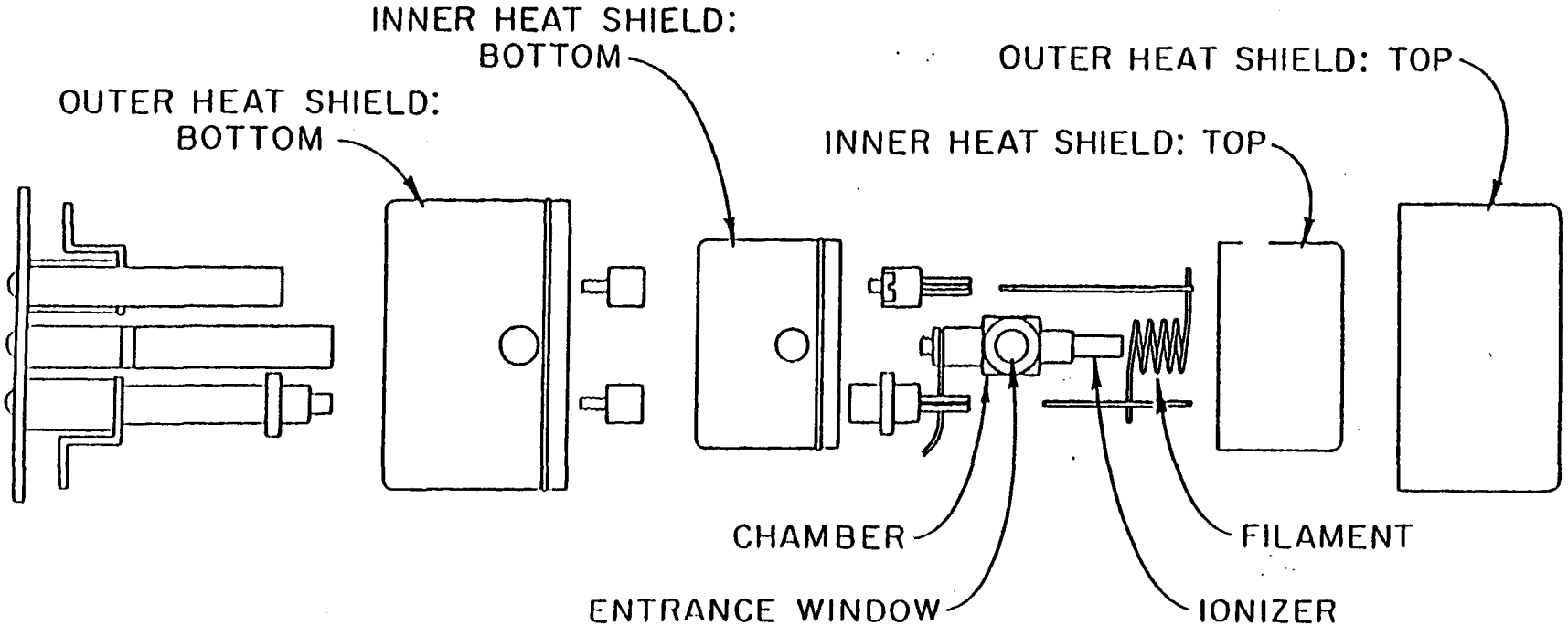

Figure 10. UNISOR surface ionization ion source.

duced nuclei recoil through a target foil window into the source body reaction chamber. The source body is heated by an electron bombardment current (approximately 300 mA at 2 kV) from an electron supplying filament, a 40 mil tungsten wire helix about the ionizer. The axes of both helix and ionizer lie on the extraction axis. Thermal radiation from the filament also serves to heat the source body. The hollow ionizer and source body are constructed of tungsten, or, in another version, graphite, due to their high melting points and high work functions (> 4.3 eV or tungsten and carbon). In the two available versions the ionizer and source body are heated to greater than 1000°C and provide good surfaces for surface ionization. Once ionized the ions are extracted electrostatically through the extraction orifice at the tip of the ionizer.

The high temperature ion source, shown in Figure 11, uses an electron bombardment current to heat either a plasma or the reaction chamber, or both, to temperatures above 1100°C. As in the SIS, the compound nuclei recoil through the target foil into the body of the ion source. The interior surfaces of the source, constructed of graphite, are sufficiently hot to surface ionize adsorbed atoms. Once ionized, the atoms are electrostatically extracted through an extraction orifice at the top of the HTIS body.

Several heat shields are sued on the SIS and HTIS to provide thermal isolation for the source from its surroundings, and to protect the structural integrity of the ion source housing.

The extracted ions were mass separated using the UNISOR Danfysik mass separator, shown in Figure 12. The separator is capable of mass resolution on the order of $\Delta m/m$ 2000. An acceleration potential of up

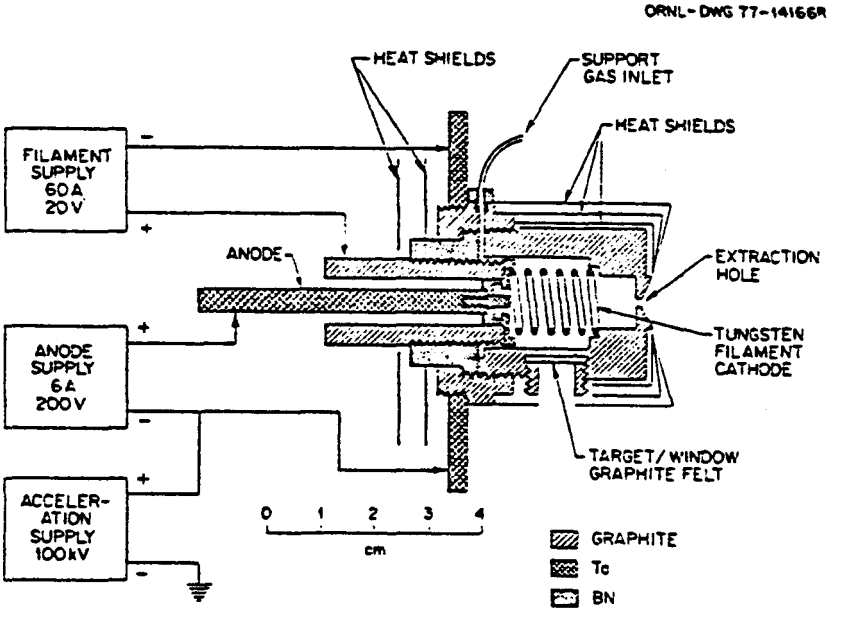

Figure 11. UNISOR high temperature ion source. Materials used in in construction are indicated, as are electrical connections.

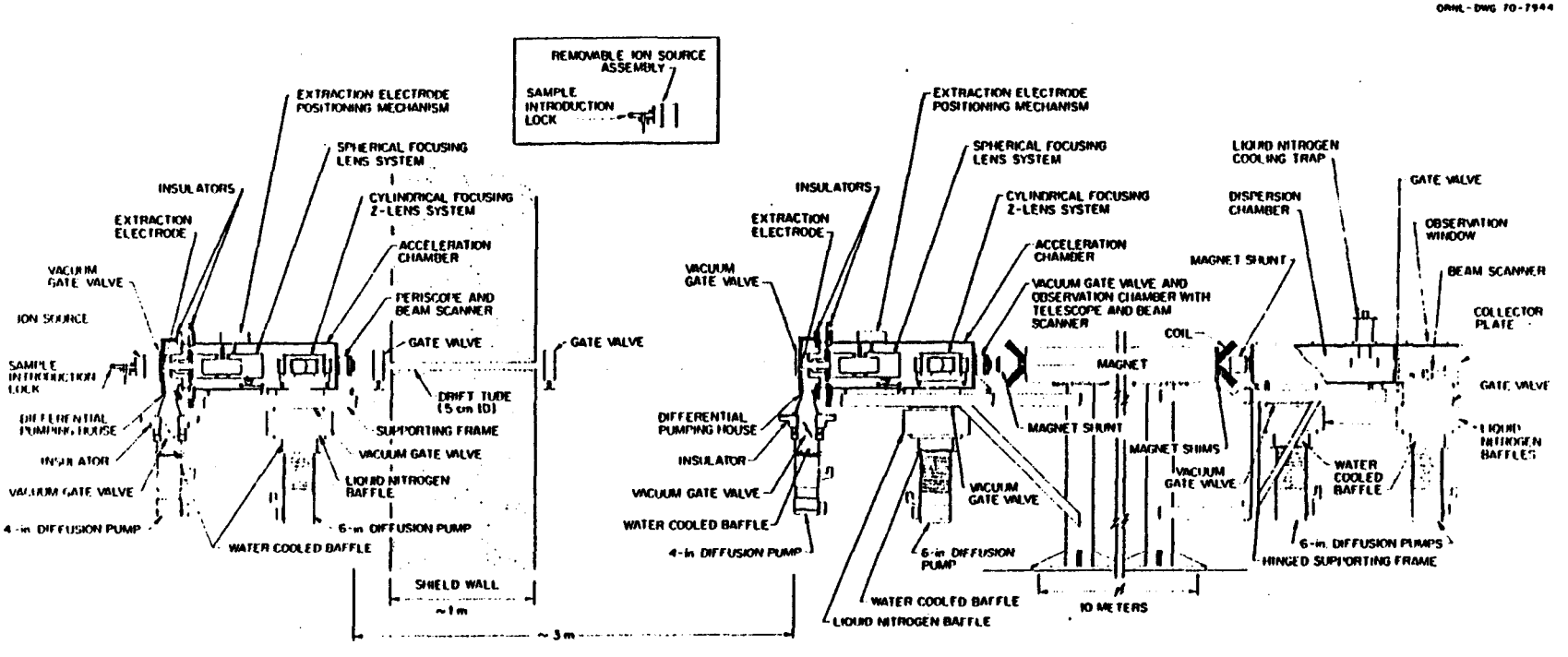

Figure 12. Mass separator similar to the UNISOR separator. The UNISOR separator does not have the cylindrical focusing Z-lens systems.

to 100 kV may be applied to the extracted ions prior to entering the 1.5 m radius of curvature, 90 degree sector, analyzing magnet. The separated masses are directed into a collection chamber containing a "flying wire" beam monitor which monitors beam position and intensity. Each of three beams of interest can be electrostatically deflected down individual beam lines maintained at high vacuum ($< 10^{-5}$ torr) by turbopumps.

The selected isotope beams impact on a collection tape of aluminized mylar or magnetic recording tape. The tape is then moved so that the deposited material is in front of the radiation detectors while another source is being deposited. The collection times are generally chosen to be approximately three times the half-life of the parent isotope of the nuclei to be studied. Positioning is accomplished by rapid stepping motors operated by pre-set indexing controllers. These controllers are triggered using signals from the data acquisition computers.

In some cases, the beam current striking the tape can be monitored to aid in tuning the separator. In general, the electric currents of the radioactive beams are not large enough to be readily measured, being well below one picoampere in most cases. As a standard alternate method, the radiation intensity at the deposition site of the central beam line was monitored by a Na(I) detector and associated electronics. The optics of the separator were then adjusted to maximize the radiation intensity after initially tuning up on a stable mass nearby, whose beam current was measurable.

C. Radiation Detectors and Associated Electronics

The detectors used in this study were all large volume, liquid nitrogen cooled lithium drifted germanium and silicon semiconductor detectors, with the exception of those used for alpha measurements, which were room temperature surface barrier detectors. Detector arrays were calibrated as described below for absolute efficiency. The gamma detectors were high efficiency Ge(Li) detectors with energy resolutions of 2.1 keV or less at 1.33 MeV gamma ray energy.

A typical electronics set-up in the experiments used a high voltage bias supply for the detector, with a preamplifier (whose first stage incorporated a liquid nitrogen cooled FET for noise reduction) feeding its signal directly to a linear amplifier and a timing filter amplifier. The spectroscopy amplifier was adjusted to provide optimum energy resolution. The timing filter amplifier was set to optimize the timing resolution; its output was fed into a constant fraction pick-off discriminator which produced a logic signal for each event detected above a pre-set threshold.

D. The UNISOR Data Acqusition System

Data acquisition at UNISOR was performed by Tennecomp TP-5000 pulse height analysis computers, two of which were on site with a third available by cabling in another section of the ORIC building. These computer systems have been described in detail elsewhere.[32] A cursory review of the structure of the system for taking coincidence data is given here. A schematic of such a set-up is given in Figure 13.

In addition to the linear energy signal from the spectroscopy amplifier and the logic signal from the constant fraction discriminator

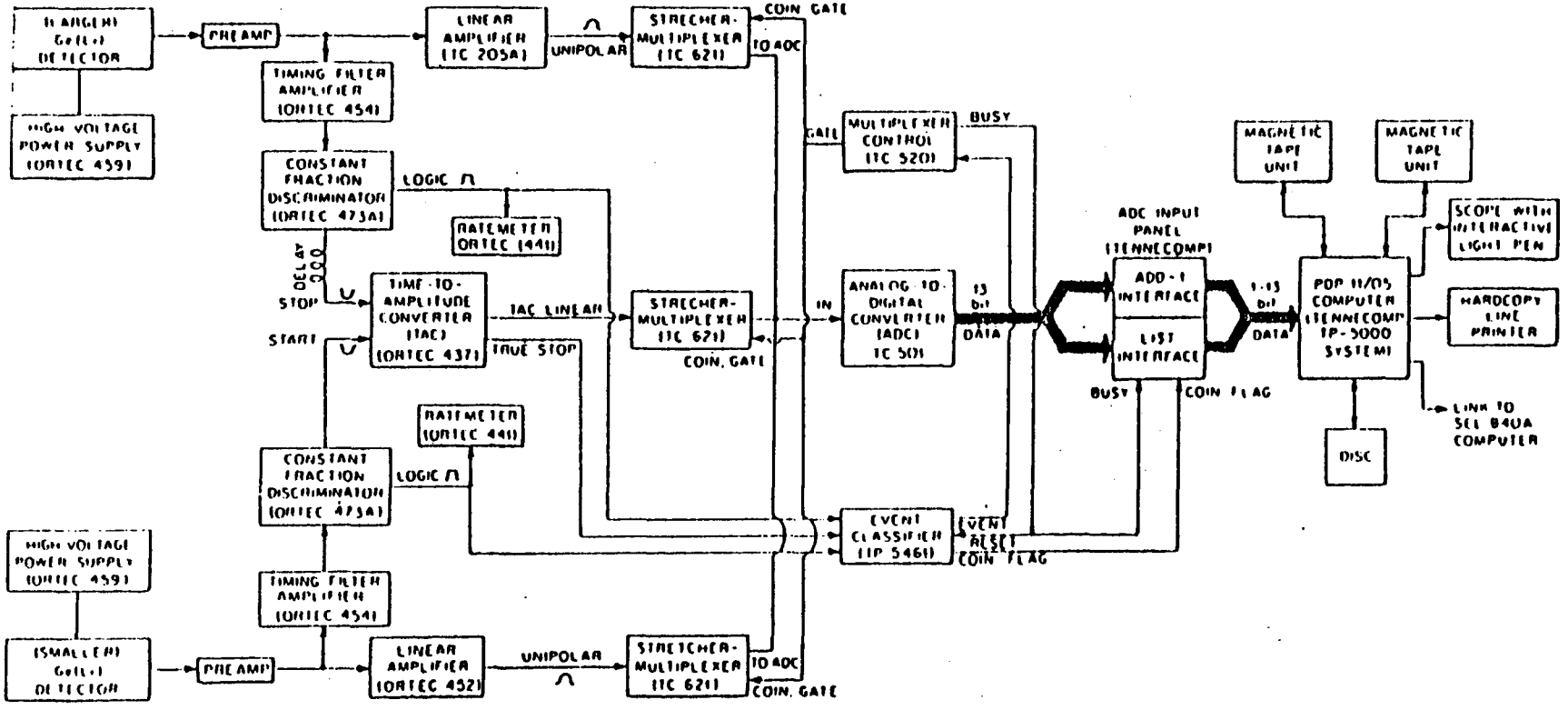

Figure 13. Schematic diagram of the electronics for a typical gamma-gamma coincidence experiment using the UNISOR data acquisition system. The ratemeters shown are used only occasionally but are shown connected as they normally would be during an experiment.

mentioned above, coincidence studies with the TP-5000 systems required another signal proportional to the time between two events registering in different detectors of the coincidence detector array. This was accomplished with a time-to-pulse-height converter (TPHC or TAC, for time to analog converter), which received the logic signals from the two constant fraction discriminators. One of the detectors was designated the "start" side of the coincidence system; the detector so designated generally had the higher count rate of the two detectors in the system.

The logic signals from these detectors were fed into the TPHC, whose circuitry then generated a signal with a pulse height proportional to the time between events. This signal was passed on to the TP-5000 system, carrying an analog of the time between the two events in the two detectors, and was used to determine if the two events were in coincidence, delayed coincidence, or were uncorrelated with each other.

If no "stop" signal was received before the range of the TPHC was reached, the TPHC reset itself internally and waited for the next "start" signal. The timing range was set for 400 nsec for all of the coincidence studies in this experiment, since this was sufficient to include delayed coincidence events for any isomeric states in either of the nuclei being studied. The TPHC's used were designed to produce a logic signal when the time between the two events was less than 400 nsec.

The TPHC spectrum was adjusted so that the "prompt" (i.e.: nearly zero time between events or "coincident") peak in the spectrum was centered in the TPHC histogram. This was accomplished by inserting delay cable into the "stop" side of the coincidence systems. Each TPHC spectrum then had three regions: (1) the region to the left of the prompt peak,

encompassing those events where a "stop" event preceeded a "start" event; (2) the region to the right of the prompt peak, where a "stop" event followed a "start" event; and (3) the prompt peak region, where the two events were nearly coincident.

The energy and time analog signals were multiplexed into an analog-to-digital converter (ADC), which in turn passed these signals on to the computer for storage in an "add-1" or histogram fashion. When received by the event classifier, the TPHC logic signal caused the "list" interface to pass the digitized energies and time signals for the two coincident events to a storage buffer in the computer. When this buffer filled, the data contained in it were dumped onto magnetic tape. This three parameter list data was analyzed in a manner described below.

The TP-5000 systems possess software which permit the computers to control many of the sequencing tasks for the experiments, such as starting and stopping ADC's, moving collection tapes, and manipulating beam stops. The computers also are able to store the "add-1" data in multiscale fashion: Successive histograms are generated from a single deposition by counting for equal fractions of the source deposition time and storing each of the histograms created. When the next source is moved to the counting position, the histograms are read from memory in sequence and added to the new data for the next multiscale cycle. From these multiscale spectra, half-lives can be determined from the observed lines.

One of the TP-5000 systems is able to transmit data to either of the two SEL 840A computers located within the ORIC facility for more detailed analysis than the basic software of the TP-5000 systems permit. Additionally, software packages have been developed which allow data to be analyzed by the Oak Ridge National Laboratory IBM 360 series computers.

E. Calibration of the Detector Systems

Each detector system used for the experimental program was calibrated for energy and efficiency over a broad range of energies during each experiment. Standard reference radioactive sources from the National Bureau of Standards, consisting of mixtures of isotopes possessing radiations with accurately known energies and activities, were used. These sources were placed at the position where the isotopes for study had been positioned during counting (the "source position"). By observing these standard sources in source position the gain, linearity, and efficiency for each detector of the detection systems were accurately determined.

A mixed ^{133}Ba and ^{207}Bi open source was used for calibrating the electron and gamma detectors used to determine internal conversion coefficients. Separate open alpha particle sources of ^{240}Pu and ^{244}Cm were used for calibrating the alpha detectors, and a mixed NBS source (consisting of ^{57}Co, ^{60}Co, ^{85}Sr, ^{88}Y, ^{109}Cd, ^{113}Sn, ^{137}Cs, ^{139}Ce, and ^{203}Hg) was used for calibrating the gamma detectors. These sources possess radiations whose energies spanned the regions of interest in these experiments (approximately 20 to 1200 keV, 30 to 2000 keV and 5 to 7 MeV for the electron, gamma, and alpha detectors, respectively).

Very accurate gamma ray and alpha particle energies for the nuclei under study were obtained by placing the appropriate reference material atop or immediately adjacent to a deposited source and then counting for some time. The resulting spectra then contained both the standard lines and the lines from the nuclei being studied with calibration source position effects minimized. The counting periods for these "accurate

energy" experiments were of sufficient length to achieve small statistical errors on all but the weakest peaks, and enabled the determination of the gamma and alpha ray energies to better than 0.1 and 7 keV, respectively, for well separated peaks.

The time conversion gain of the time-to-pulse height converter was determined for the individual experiments by one of two methods. The more accurate method used a commercially available pulse generator with selectable delay between two outputs which were connected to the "start" and "stop" inputs of the TPHC. The delay was increased in steps while a TPHC output spectrum was taken, giving a series of evenly spaced time delay peaks across the range of the conversion. The second method used the detection system outputs of the coincidence array, with an intense source in the source position. Long lengths of delay cable were introduced alternately in the "start" and "stop" sides of the timing set-up to obtain time-displaced peaks in the TPHC spectrum. By converting the delay line length into nanoseconds, a time conversion gain could be calculated.

The TP-5000 histogram storage buffers could accommodate 8192 channels of histogram data. For these experiments, histograms were typically of 4096 channels in length, requiring the storage of most multiscale histograms on the disks of the computers. For very short multiscales (less than one second per plane), the disk access time became a significant factor in the data taking cycle. To provide time normalization for these multiscales either a pulser output applied to the preamp input of one of the detectors or a strong line from background radiation, or both, were used to provide time normalization to the multiscale spectra.

With the techniques described in this and the preceeding sections of this chapter, it is not unusual for the system to process and store in some fashion several million events during the course of an experiment. The analysis of this mass of data requires special techniques which are described in the next section.

F. Internal Conversion Electron Spectroscopy

The de-excitation of an excited level in a nucleus takes place by an electromagnetic interaction which transfers excitation energy and angular momentum from the nucleus to an electromagnetic field. Though the field may produce a photon with the energy and angular momentum of the field, those conserved physical quantities may instead be transferred to an atomic electron. The orbital electron is then ejected from the nucleus with kinetic energy equal to the difference of the energy of the field and the binding energy of the electron; the electron is then said to have been internally converted. The internal conversion electron must also carry off the angular momentum of the field. As in all electromagnetic interactions, the total parity of the system must be conserved throughout the process.

The conservation of energy, angular momentum, and parity dictates the relative competition between the modes of electromagnetic decay, and the theory of these processes has been extensively developed. As a result, the measurement of the ratio of internal conversion electrons to gamma rays emitted for a particular transition in a nucleus provides a powerful tool for nuclear spectroscopy, identifying the changes in spin, parity, and energy for a transition. The ratio is called the

internal conversion coefficient and these are generally calculated theoretically using the algorithm of Hager and Seltzer.[33]

The calculated internal conversion coefficient (ICC) may also be broken down into atomic electron subshell (K, L, M, . . .) conversion electron-to-gamma ray ratios. Measurement of the experimental ICC's for the K or L subshell is often sufficient to determine the multipolarities of the nuclear transitions. If the character (multipolarity) of the transition is mixed, a mixing ratio δ^2 may be deduced for the ICC, defined to be the ratio of the intensities of the multipole components of the transition. (An alterhate method of defining δ^2 is given in reference 34.)

The internal conversion coefficients for transitions in the nuclei studied here were made with a Ge(Li) gamma detector and a Si(Li) electron detector, both cooled to liquid nitrogen temperatures, in a calibrated geometry. Peaks in the gamma and electron summed multiscale spectra were analyzed as described in Section I. The pure E2, $2^+ \rightarrow 0^+$, (first excited to ground state) transition in the neighboring even-even polonium nuclei provided a normalization factor for the experimental ICC's. Such a normalization was essential to properly correct the experimental data for systematic uncertainties such as live time differences between gamma and electron detectors, absolute counting geometry and other undetermined factors.

G. Alpha Branching Ratio Measurements

Often nuclei far from stability have several competing modes of radioactive decay. The francium nuclei with $N < 126$ primarily decay by alpha particle emission, but also decay at a considerably lower rate

via electron capture or positron decay. The ratio of the alpha decay intensity to the intensities of the other modes of decay for a given nucleus is called the alpha branching ratio.

The measurement of francium alpha branching ratios for these experiments were made with a Ge(Li) gamma detector opposite a surface barrier alpha detector in a calibrated geometry. In the studied radon daughter nuclei, no transitions were observed in the radon nuclei which bypass the first excited to ground state transition ($2^+ \rightarrow 0^+$), as will be noted in the subsequent chapter. The measurement of this transition intensity, which is the gamma intensity corrected for E2 internal conversion, and the simultaneous measurement of the alpha intensity of the decaying parent nucleus provides a straightforward or accurate method of measuring the alpha branching ratios.

Previous measurements of the francium alpha branching ratios by other groups deduced them by observing only the alpha decays of the parent and daughter nuclei. The alpha branching ratios were assumed to be well measured for the daughters and thus their intensities would permit deduction of the parent alpha branching ratio. This assumption, however, represents a fundamental systematic weakness in such an approach, for there is some disagreement in the reported values for the astatine and radon alpha branching ratios. Additional uncertainty is introduced by the recoil of the alpha decaying nuclei from the source for study. The recoiling nuclei possess sufficient energy to travel some distance before decaying, thereby disturbing the calibration geometry for the detection systems.

Since the method used here does not require assumptions concerning the daughter decay properties and precludes recoil effects on the

system calibration, the method employed here represents an improvement over those used previously.

H. Level Half-Life Measurements

If the lifetime τ of an excited radon nuclear level was between about one to several hundred nanoseconds, the coincidence systems used were able to ascertain the half-life of that level. Three techniques were used; all compared differences between generated TPHC spectra with gated transitions above and below the delayed state (delayed spectra) to TPHC spectra generated by similar gates on very short lived levels (prompt spectra). These techniques are discussed briefly here; more detailed descriptions may be found elsewhere.[35]

Ideally prompt TPHC spectra are very narrow Gaussian peaks about some point in the range of the TPHC. The TPHC spectra is viewed as a plot of events versus time; the centroid of the prompt transition may be called t_{prompt} or t_p. To the left of this point, stop transitions must precede start transitions in the coincidence data to generate a TPHC event; the inverse is true of the right side. When a state decays with a lifetime within the range noted above the prompt peak will be distorted by the exponential decay of the state. If P(t) represents the prompt peak height at t, the delayed portion of the peak may be written as

$$F(t - t_p) = \frac{1}{N} P(t - t_p) \exp [-\lambda(t - t_p)]$$

where $F(t - t_p)$ is the delayed channel height at t, λ the level decay constant and N is a normalization factor. In this formula the direction of t must be such that $t > t_p$.

If the width of P was much less than τ, the slope of the decay portion of the delayed spectra was equivalent to λ and immediately related to τ. This method, called the slope method, is only accurate when τ is much greater than the width of P.

When τ was only somewhat greater than the width of the prompt peak, two other methods were used. The redistribution of the prompt peak intensity by the exponential decay function shifts the centroid by an amount Δt. This centroid shift may be related[36] to the half-life by $\tau = \Delta t \ln 2$. A more detailed study of the peak may be made by deconvoluting the function P by the relation

$$F(t - t_p) = \frac{1}{N} P(t - t_p) \exp(-\lambda(t - t_p)) \quad .$$

Since F and P are known, and N merely conserves area in the peaks, λ may be varied to yield the best fit to the data by a one parameter fit algorithm. A computer program was written which performed this fit. In all cases centroid shift and deconvolution values for level half-lives were equal within experimental error.

I. Data Analysis Techniques

The data analysis techniques used for these studies fall into the following broad categories and will be discussed in that order: photopeak centroid and intensity determination; half-life estimation; deduction of coincidence logic; coincidence intensity analysis; live time corrections; and elimination of summer effects.

Peak centroids and intensities were initially calculated using the computer program LIZA,[37] which is resident on the SEL 840A computers at the ORIC facility. The routine fits the peaks with a Gaussian shape,

and can simultaneously fit up to five peaks. The routine yields the centroids, areas, and probable errors from the Gaussian fitting procedure.

It should be noted however that semiconductor detector photopeaks do not exhibit perfectly shaped Gaussian line shapes[38] due to charge collection effects and, in the case of charged particle detectors, energy straggling. Several peak fitting programs take this into consideration and fit one or more decaying exponential functions to the high and low energy limbs of the peak, whose basic shape is generally taken as a Gaussian.

The peak-fitting routine used for the final data analysis for these experiments was a version[39] of SAMPO. The version used, resident on the Oak Ridge National Laboratory IBM 360 and 3033 series computers, first performs a best fit analysis of several strong, well separated peaks spaced across the spectrum. The fitting parameters obtained for these peaks were observed to vary smoothly with energy. The program then calculates a linear interpolation of these fitting parameters throughout the spectrum and uses them to perform a peak search on the spectra to be analyzed. The program uses a Gaussian line shape augmented by high energy and low energy exponential tailing functions attached to the Gaussian peak. An automatic fitting to the peaks found in the peak search routine is performed. In most cases, a more controlled peak search and fitting procedure was needed, for which the program has provisions. The version used allowed peak selection, background determination specification, and choice of peak "significance level" during the search. The results of the fitting process are printed out graphically as well as in tabular form to assist in determining the quality of the fit.

The SAMPO program also calculated centroid and intensity errors based on the fits to the spectra. The program calculated the error based on three sources: (a) the error associated with the efficiency calibration which was assumed to be 5%, (b) the statistical error associated with the area calculated for the peak by the fitting procedure, and (c) the statistical error associated with the peak centroid. When centroids were used to determine energies the error in the linear interpolation to the detection system gain was also entered in the computation of the error. The errors obtained are those which are quoted in the tables for photopeak intensities and energies.

SAMPO, in conjunction with the calibration methods described previously, can deduce peak centroids to better than 0.1 channel in many cases. Thus, comparable accuracy in determining the energy of the peaks required determination of the non-linearity of the ADC systems. In addition to measuring the non-linearity of the various ADC's used in the experiments with the multiple source technique,[40] which found the non-linearity to be less than one channel throughout the spectrum, SAMPO performed a polynomial fit to the spectra obtained in the accurate experiments to determine the peak energies to 0.1 keV or better in most cases.

The photopeak intensities in each multiscale plane could be observed to determine the half-life of the isotope in which the transitions were located. Since the multiscale plane durations were chosen to optimize the source activity for francium production, the much longer half-lives of the radon and astatine nuclei following the francium decays could not be determined with precision. The francium half-lives were determined by noting the decay in the alpha peak intensity in the

multiscale planes, where far superior statistics to the gamma information were available. A Poisson-weighted, least-squares fit to the alpha intensities in the multiscale data was performed.

The three parameter (gamma-gamma-time, or electron-gamma-time) list data were analyzed with the Tennecomp systems to establish the coincidence relationships for the transitions. This was done by scanning the magnetic tapes and generating histograms with restrictions on the allowable ranges of two of the parameters. These restrictions referred to as "gates," were the upper and lower boundaries of lines observed in the summed multiscale data and the prompt peak of the TPHC. These limits were used to gate the opposite detector. The prompt peak range was on the order of 15 nsec for all peaks generating prompt gates. All gated spectra from opposing gamma detectors were gain corrected and added together to enhance statistics for weak lines.

TPHC limits were also taken on either side of the prompt peak to determine the ordering of transitions occurring about isomeric states in the two nuclei studied. By specifying the time limits and the particular detector, the time delay between states above and below an isomeric level caused clearly recognizable intensity differences between spectra gated on different sides of the TPHC.

The deduced coincidence relationships between the gated gamma transitions were used in conjunction with the energy and intensity measurements to construct the level schemes for the radon nuclei under study. Feeding to levels directly from the parent francium nuclei could be determined by noting the discrepancies between transition intensities into and out of each level, with corrections made for internal conversion. Such "intensity balancing" also can point out

defects in the constructed scheme. If a level appears to possess greater intensity populating than depopulating it, the level must be scrutinized for missing de-excitation transitions, isomerism, or improperly assigned feeding, for instance. Such a technique, then, is a very useful method of testing the validity of the constructed level scheme and deducing the presence of doublets.

An additional test to that of intensity balancing was coincidence gate intensity balancing. In this technique the transition intensities within gates were determined and compared with expected intensities deduced from the constructed decay schemes.

The coincidence intensities may be calculated by correcting for branching (to and from levels in the proposed decay scheme) above or below the gated transition, internal conversion, and detector efficiency. This method allowed a checking of each decay scheme after regular intensity balancing. It was also useful in deducing the presence and intensity of doublets and their components or lines whose intensities were masked by background radiation.

In the several coincidence experiments performed, corrections were made to the observed summed multiscale spectra to account for true coincidence summing effects. The method used[41] applied the formula:

$$I_{\text{sum peak}} = A p_1 p_2 \varepsilon_1 \varepsilon_2$$

where A was the source activity, and p_i and ε_i were each of the sum peak components' emission probability and detection efficiency, respectively. With the approximate intensity determined by this equation and the information from the coincidence gates, summing effects were taken into account in computing intensities for the observed lines.

CHAPTER 4

OBSERVATIONS OF THE DECAY OF MASS-SEPARATED ^{208}FR AND ^{206}FR

A. Introduction

The isotopes ^{208}Fr and ^{206}Fr were mass-separated at the UNISOR facility using the surface ionization and high-temperature ion sources. A series of five experiments were performed which are outlined in Table 2. The following types of data were taken: simultaneous alpha and gamma multiscale, simultaneous gamma and electron multiscale, and gamma-gamma and gamma-electron coincidence. Additionally, accurate energies were determined for the alpha and gamma radiations using the standard source technique discussed in Chapter 3.

Half-lives were determined from the decay of the alpha decay intensities in the multiscale spectra. The gamma ray data provided confirmation of those values deduced from the alpha decay observations. All calculated half-lives agreed very well with those previously reported, as did all determined alpha decay energies[10,11] (excluding the heretofor unobserved isomer in ^{206}Fr).

Much more ^{208}Fr than ^{206}Fr was produced following the heavy ion reaction used in these experiments. This, coupled with the higher alpha branching ratio and shorter half-life of ^{206}Fr, resulted in much greater detail in the observations of the decay of ^{208}Fr than ^{206}Fr. The observation of these decays are presented below, with ^{208}Fr discussed

first. The correlation of these observations with those of other groups will be presented in Chapter 5.

B. The Decay of ^{208}Fr

1. Alpha Decay

The single alpha decay group in ^{208}Fr was found to have an energy of 6.636 ± 0.005 MeV and yielded a half-life of 58.1 ± 0.3 seconds. The daughter nuclei, ^{204}At and ^{208}Rn, also alpha decay and the decay energies were determined to be 5.946 and 6.147 ± 0.005 MeV, respectively. The multiscale data for all ^{208}Fr experiments were of 150 seconds total duration which precluded measurement of the reported[42] much longer half-lives of the daughter nuclei. A sample of the summed multiscale data for the alpha observations is shown in Figure 14.

Using the method described in the previous chapter, the alpha branching ratio for ^{208}Fr was determined to be 89 ± 3%.

2. Electron Capture Decay

The gamma ray multiscale data taken simultaneously with the alpha measurements discussed above were used to identify the strongest transitions associated with the electron capture decay of ^{208}Fr by their half-lives. The strong lines were used as initial gating parameters for analyzing the gamma-gamma coincidence data. The characteristic x-rays of radon were observed in these gates, confirming their assignment to the decay of ^{208}Fr. These gates in turn disclosed more transitions within ^{208}Rn. Eventually almost all lines in the multiscale spectra were identified as belonging to ^{208}Rn, ^{204}Po (populated by the electron capture decay of ^{204}At), or background radiation. The gamma ray gates for transitions identified for radon are shown in Figure 15. The

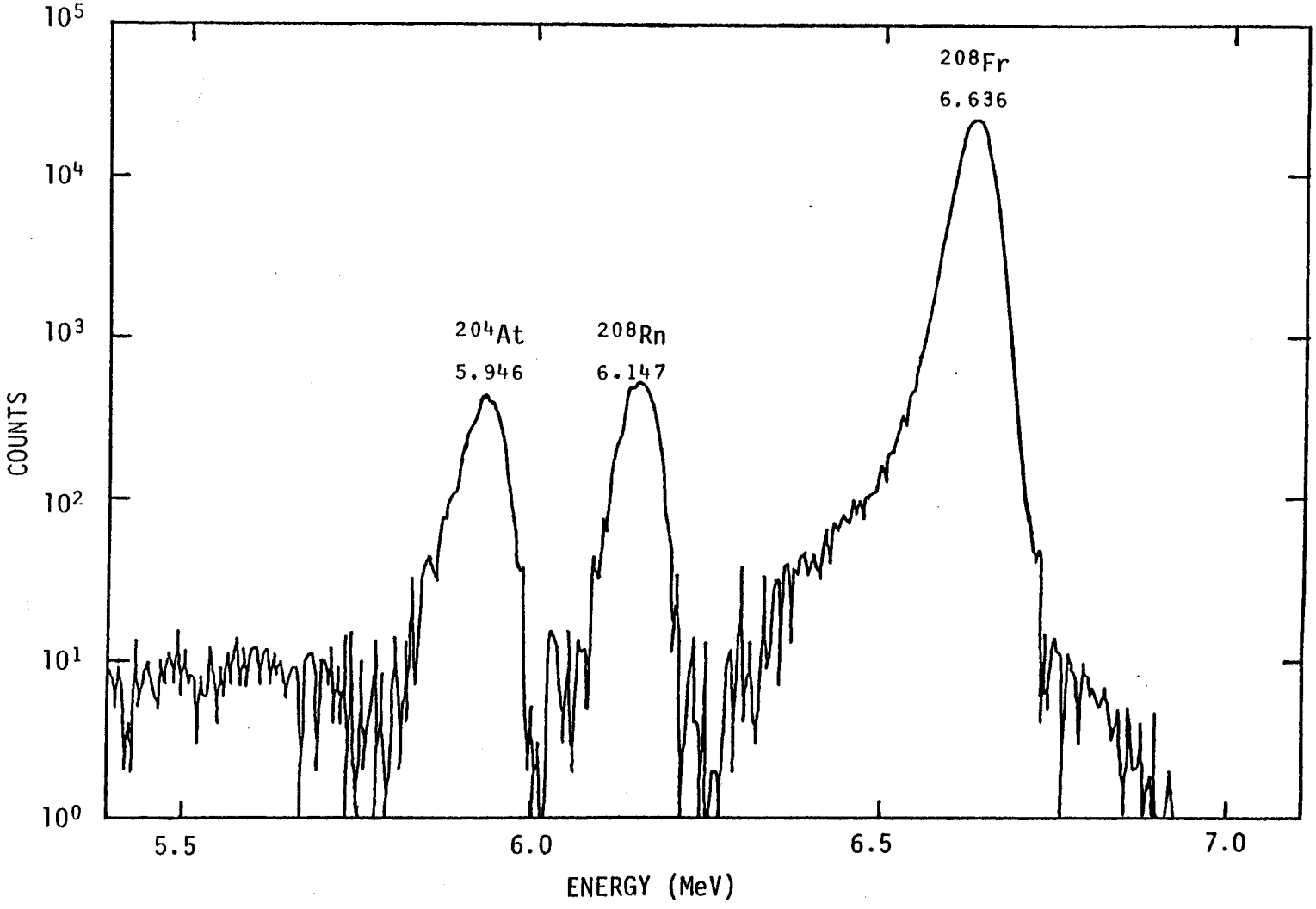

Figure 14. Summed alpha multiscale spectrum for the decay of ^{208}Fr. Energies are in MeV.

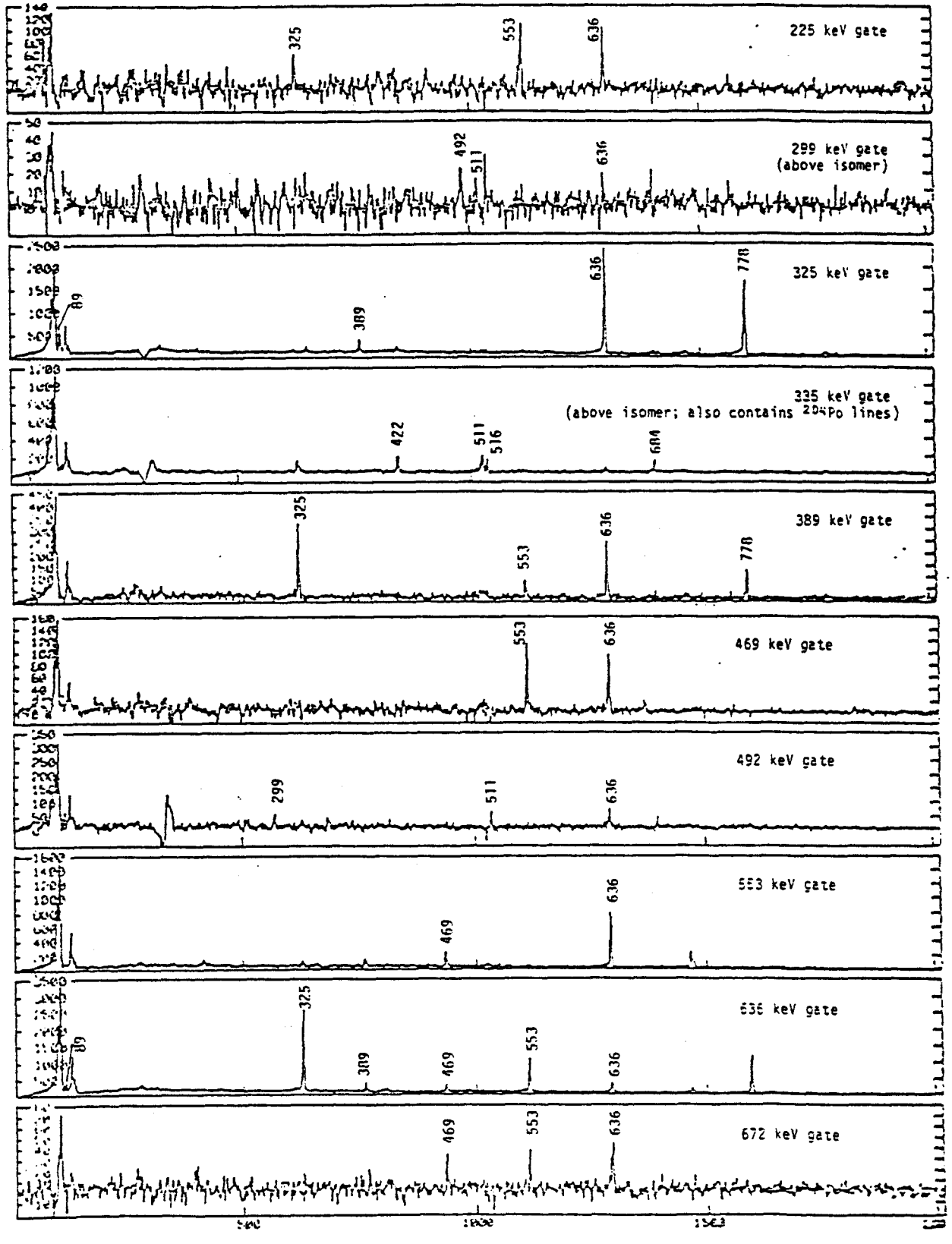

Figure 15. (caption on next page)

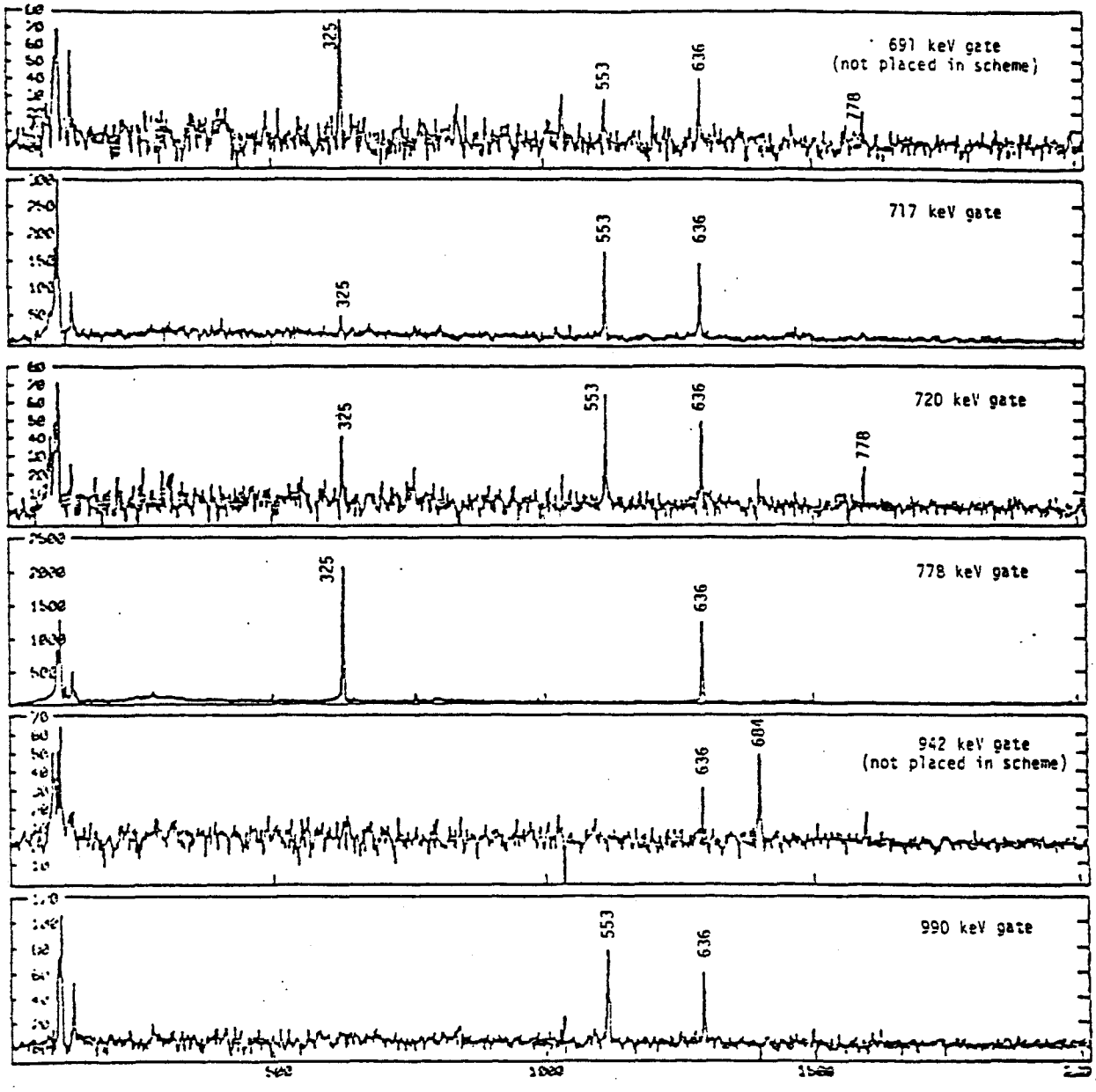

Figure 15 (continued). Gates on transitions in ^{208}Rn. Energies are in keV. A strong 335 keV line exists in both ^{204}Po and ^{208}Rn.

gamma-electron data provided additional corroborative evidence for the coincidence relationships, which are summarized in Table 3.

The gamma and electron multiscale data permitted the determination of the internal conversion coefficients for the most intense transitions. An exemplary summed multiscale for each is shown in Figure 16. The electron data disclosed no evidence for any E0 transitions. All transitions for which multipolarities could be deduced from the ICC determinations are of M1 or E2 character, neither of which change the parity of the nuclear system. The transitions for which ICC's were determined are all connected to the ground state directly or via other transitions for which ICC's were measured. Thus all levels connected by these transitions have the same parity as the ground state, positive.

A summary of the data obtained for all transitions within ^{208}Rn is given in Table 4. Energies quoted in that table are from the accurate energies measurements as previously stated. The intensities come from the SAMPO analysis of the summed multiscale data, with the exception of those for the 389 and 636 keV doublets and the 88.9 keV transition which are discussed below. All intensities are corrected for coincidence summing effects, which were less than 3%.

Based on the above discussion and the information in Figure 15 and Tables 3 and 4, the decay scheme shown in Figure 17 was deduced. The ordering of the transitions and levels is based on the observed singles intensities and the results of the accurate energy technique. The scheme was determined to be energy and intensity balanced throughout. Further confirmation of the scheme was provided by a coincidence intensity analysis; the results obtained for several of the transitions are given in Table 5 and reflect the general agreement found for all

Table 3. Coincidence relationships established by gamma-gamma gates for ^{208}Rn transitions. "x" denotes appearance of given line in gated spectra. "?" denotes marginal significance. Only gates with adequate statistics to deduce coincidence relationships are shown.

Gated energy (keV)	Gamma energy (keV)																		
	89	225	299	325	335	389	470	492	511	553	636	671	691	717	720	778	887	943	990
225				x						x	x								
299								x	x										
325	x	x			x		x		?		x			?	x	x			
335				x					x		x								
389				x					x	x	x					x			
470										x	x	x							
492			x						x										
553		x	x	x		x	x				x	x		x					x
636	x	x		x	x	x	x	x		x	x		x	x	x	x	x	x	x
671							x			x	x								
690				x					?	x	x								
717				?						x	x					?			
720				x						x	x					x			
778	x			x	x	x		x			x		x						
943											x					x			
990										x	x								

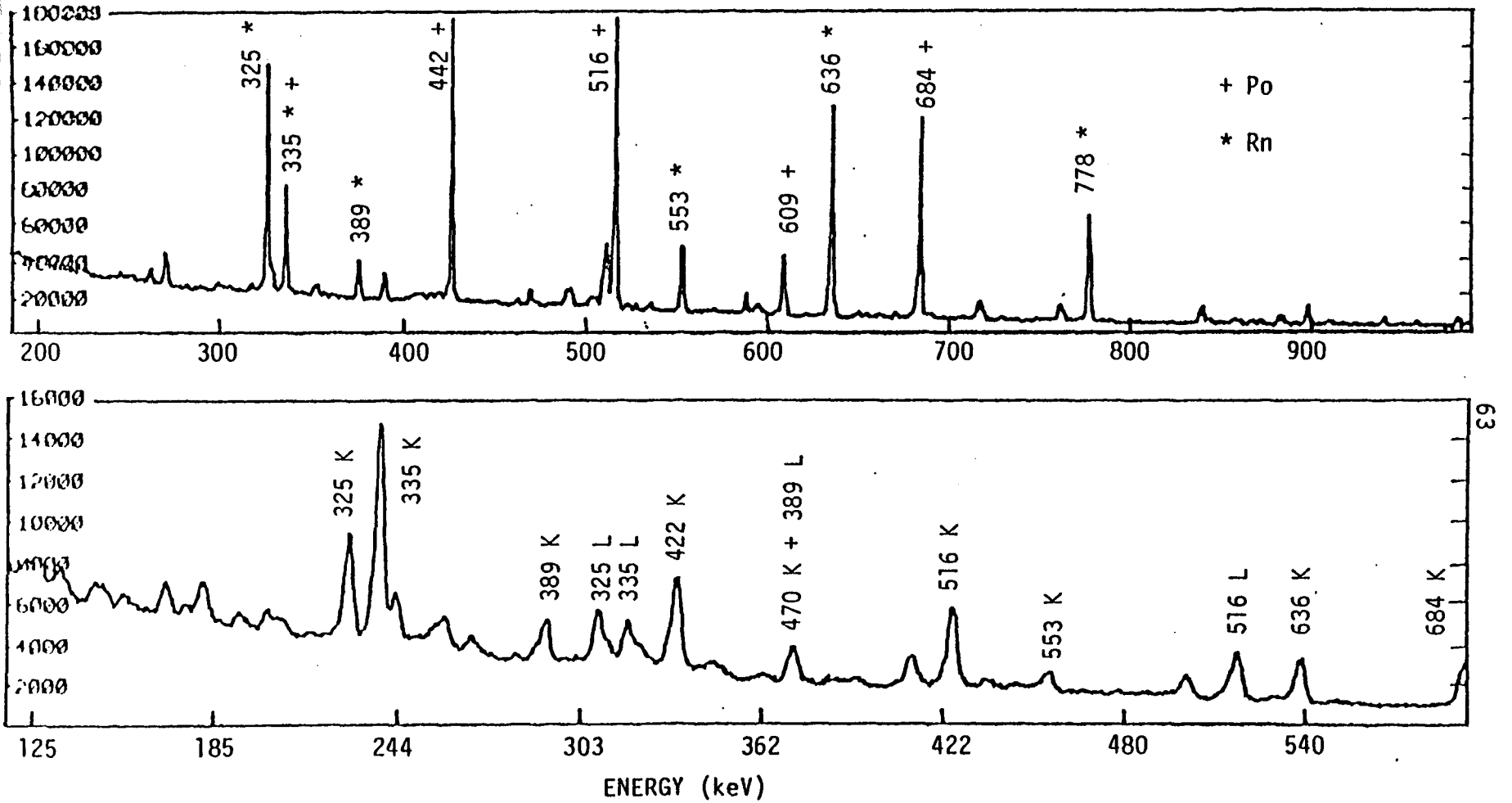

Figure 16. Example of summed multiscale data for decay of ^{208}Fr. The upper figure represents the gamma data, while the lower represents the electron data. The strongest lines are identified by energy and element, with energies in keV.

Table 4. Gamma ray transitions observed in ^{208}Rn. Theoretical internal conversion coefficients (ICC's) are from the Hager-Seltzer algorithm.[33] Energies are in keV.

Gamma ray Energy	Relative Intensity	Internal shell	Conversion Coefficient (x 10^{-2}) experimental	theoretical	Multipolarity
88.9±0.1	1.5±0.3	L	1110±170	1050	E2
225.5±0.2	0.77±0.10	K	122±12	112	M1
298.7±0.1	0.95±0.10	K	29.1±4.3	29.0	M1 + E2[1]
325.2±0.2	53.2±3.8	K	4.4±0.2	5.8	E2
335.0±0.3	12.3±5.0	K	39.5±16.0	38	M1
389.3±0.3[2]	4.0±2.2	K	27.9±10.0	25	M1
389.3±0.3	2.8±2.2	K	4.0±2.0	4	E2
469.8±0.1	5.7±0.4	K	14.6±1.5	15.1	M1
491.9±0.1	2.8±0.2	K	2.5±0.5	2.5	E2
553.1±0.1	31.0±2.2	K	1.7±0.1	2.0	E2
635.8±0.2	100.0	K	1.4±0.1	1.5	E2
636.3±0.2	6.4±2.8	K	1.4±0.1	1.5	E2
671.6±0.1[3]	1.3±0.9				
690.5±0.1[3,4]	2.2±0.2				
716.8±0.1	4.0±2.8	K	2.5±1.0	1.2	E2
719.6±0.1	6.6±0.5	K	1.1±0.2	1.2	E2
778.5±0.1	68.9±4.9	K	1.0±0.1	1.0	E2
887.3±0.1[3,4]	1.7±0.4				
942.5±0.1[3,4]	4.6±0.3				
990.1±0.1[3,4]	4.1±0.8				

Notes:
1 Mixing ratio (δ^2) is 1.0±0.2.
2 Doublet line not resolvable. ICC's are based on M1 and E2 pure components.
3 Insufficient data to deduce ICC.
4 Line could not be assigned in decay scheme.

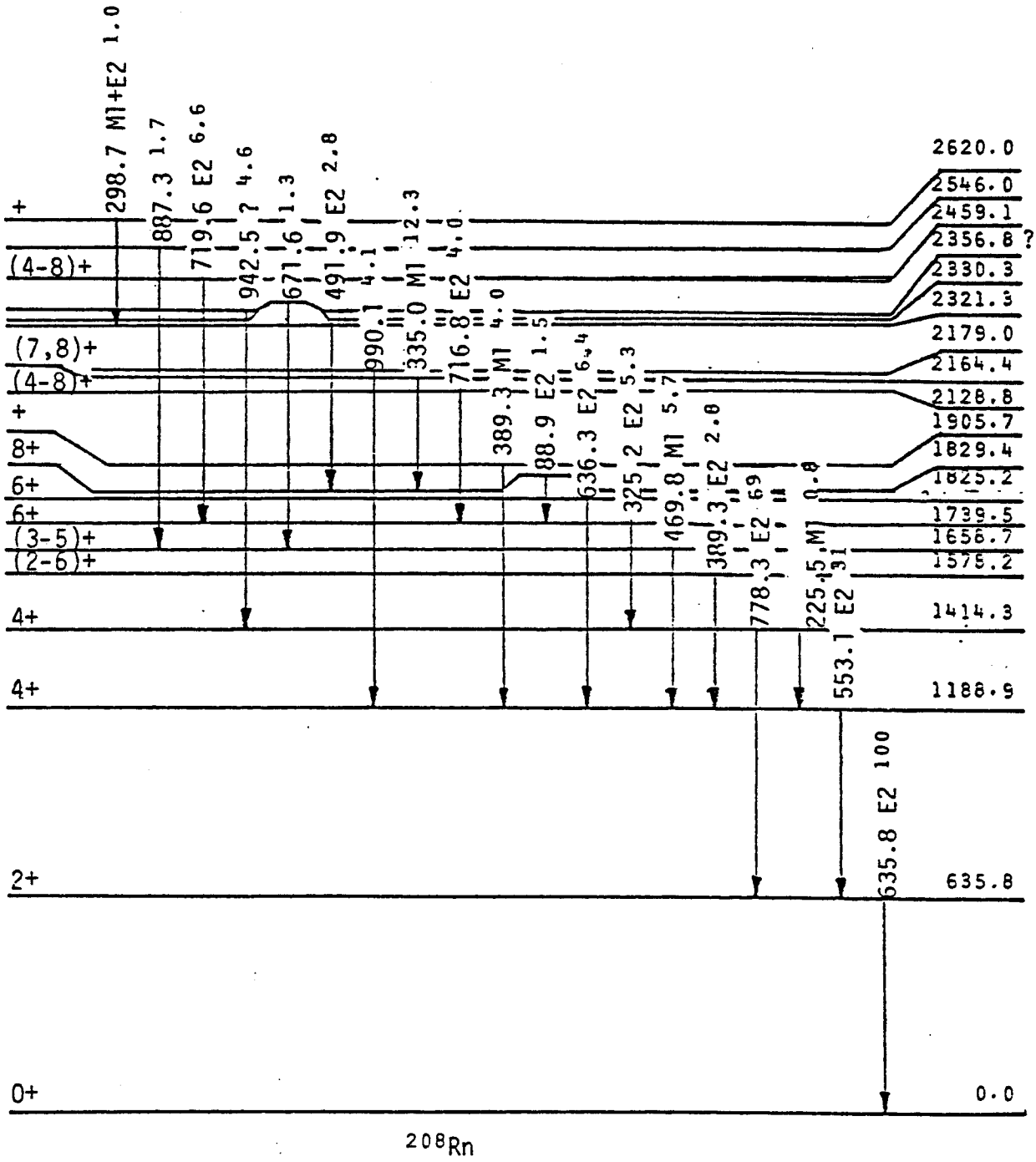

Figure 17. Deduced level scheme for ^{208}Rn. Transition and level energies are in keV. Deduced transition multipolarities are indicated. Small numbers following transition energy denote relative photon intensities. The 942.5 keV line and its associated level are suspect due to poor statistics and contamination in that gate.

Table 5. Examples of coincidence intensity analysis for selected ^{208}Rn gates. Energies are in keV; errors are approximately 25% for all intensities.

Gated Energy	Coincident Transition Energy	Relative Intensity In Gate	Relative Intensity In Gate Calculated From Decay Scheme
325	89	3.0	2.8
	225	1.9	1.4
	389	6.6	7.5
	469	0.7	0.0
	553	1.9	3.0
	635	100	100
	720	2.3[1]	12.8
	778	100	100
389	325	51	59
	511	28	-
	553	47	41
	636	100	100
	778	76	59
553	225	4.6	2.4
	325	4.4	5.2
	389	7.5	10
	469	18	18
	511	4.1	
	636	100	100
	671	3.1	4.0
	718	35[1]	13
	990	9.1	13

Notes: 1 Coincides with a sum peak; extremely difficult to ascertain intensity.

transitions. The 690.5 keV gamma could not be placed in the scheme.

Attention is now turned to a discussion of the levels in the decay scheme for which unique spin and parity assignments have been made:

a. the 0.0, 635.8, 1414.3, 1739.5 and 1829.4 keV levels - These levels represent the states previously reported by Backe et al.[2] The transitions connecting them compose the 8^+ to ground state (0^+) cascade; the E2 multipolarities for all four transitions connecting these states unambiguously yield the spins and parity for these four levels.

b. the 1188.9 and 1825.2 keV levels - The 553.1 keV gamma ray is observed to be in coincidence with the 325.2 keV main cascade gamma only through the 225.5 keV (M1) transition. Since no transitions within the radon nucleus are observed to populate the 1825.2 keV, that level must be fed directly by the electron capture decay of the ground state of ^{208}Fr. Since the spin of the francium parent nucleus has been determined[43] to be 7, the minimum physically probable spin for this level would be 6. These observations and the observed E2 multipolarity of the 553.1 and 636.3 keV gamma rays unambiguously determine the spin and parity of their associated levels.

The spins of the levels at 1905.7, 2128.8, 2164.4, and 2459.1 keV, though not uniquely determined, are delimited by the absence of feeding within the nucleus--indicating direct feeding from the parent nucleus--and the angular momentum restrictions dually imposed by the electron capture feeding from the spin 7 ground state of ^{208}Fr and by the multipolarities of their associated transitions. These limits are shown at these levels in Figure 17. All other levels for which possible spins are shown are based solely on the angular momentum restrictions

imposed by the multipolarities of the associated transitions.

It was necessary to determine the intensities of the 88.9 keV line and the components of the 389 and 636 doublets indirectly. These are discussed at this point:

a. 88.9 keV intensity - This line is swamped in the multiscale data by polonium x-rays and could not be separated from them using SAMPO. The coincidence intensity of the 88.9 keV transition in the 325, 636, and 778 keV gates yield a value for the transition intensity equivalent to 1.5 $\pm$ 0.3% of the ground state transition intensity.

b. 389.3 keV doublet component intensities - No structure is observed in this line, but evidence for the doublet structure of this line is provided by the coincidence intensity analysis shown in Table 5. From that analysis, the component intensities were deduced to be 4.8 $\pm$ 1.2% for the 389.3 keV gamma in coincidence with the 325.2 keV gamma and 2.0 $\pm$ 1.2% for the 389.3 keV gamma in coincidence with the 553.1 keV transition.

c. 636 keV doublet component intensities - Two methods were used to determine the doublet component intensities for the 636 keV doublet. Unlike the 389 keV doublet, the 636 keV line exhibits sufficient broadening to permit fitting both components with SAMPO. This fitting yielded a value of 4.2 $\pm$ 2.1% for the 636.3 keV component relative to the 635.8 keV, first excited to ground state intensity. A second method used the sum of the singles intensities of the 553.1 and the 778.5 keV transitions to predict the intensity of the 635.8 keV transition. No transition bypasses the 635.8 keV transition and only the 553.1 and 778.5 keV transitions feed the first excited state, which it depopulates. Intensity balancing thus requires that any 636 singles intensity

greater than the sum of the singles intensities for the 553.1 and 778.5 keV lines must belong to the 636.3 keV component. This method yielded a value of 8.4 ± 2.0% for the 636.3 keV gamma relative to the 635.8 line. The average value, which appears in Table 4, is 6.4 ± 2.8% for the 636.3 keV gamma relative to the 635.8 keV transition.

The half-life of the 8+ isomeric level was determined to be 347 ± 220 nsec by the slope method. The magnitude of this half-life did not permit using the centroid shift or deconvolution techniques due to the limited TPHC range used. The error quoted represents the statistical error in the least squares fit to the decay curve.

C. The Decay of ^{206}Fr

1. Alpha Decay

Figure 18 shows a typical summed alpha multiscale spectrum observed in the decay of ^{206}Fr by alpha emission. The principle alpha group in the decay was observed to have an energy of 6.790 ± 0.005 MeV. From the intensity of this group in the multiscale spectra, the half-life for ^{206}Fr was deduced to be 15.9 ± 0.3 seconds. The gamma data taken simultaneously with the alpha multiscale supported this half-life value. Half-lives for the astatine and radon decay daughters could not be determined because of the short counting periods used, as in the case of ^{208}Fr. The energies of the daughter nuclei were determined to be 6.259 ± 0.005 MeV for the radon group and 6.138 and 6.245 ± 0.005 MeV for the astatine alpha groups.

The alpha multiscale spectra also revealed the presence of an alpha group at 6.930 ± 0.005 MeV, clearly visible in Figure 18, with a half-life of 0.7 ± 0.1 seconds. This alpha group has not been ob-

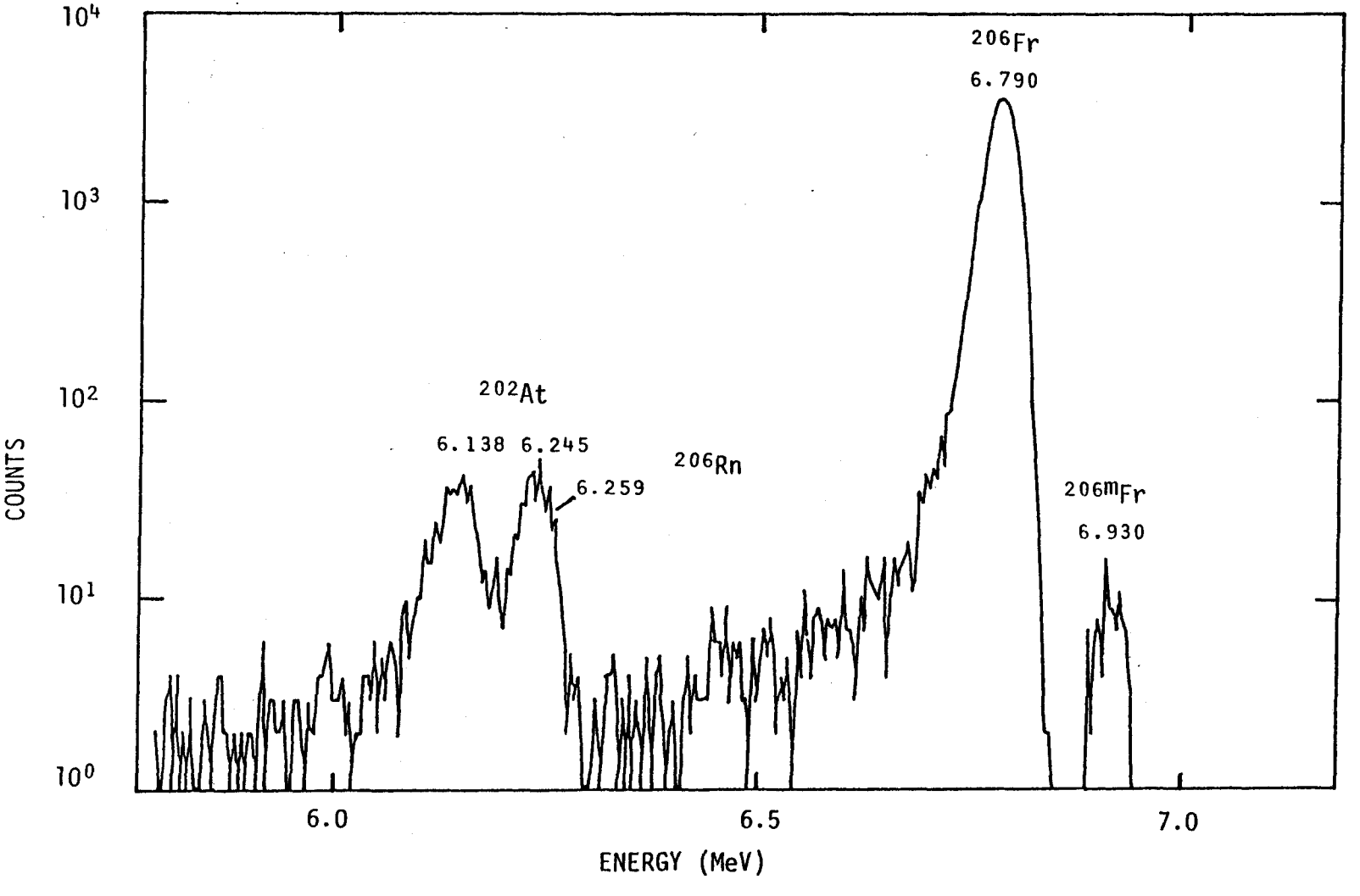

Figure 18. Summed alpha multiscale spectrum for the decay of ^{206}Fr. Energies are in MeV.

served previous to these experiments. It has been identified with the decay of a francium isomer by noting that:

a. no element with Z greater than 87 (francium) can be produced in the heavy ion reaction used;

b. the decay curve of the group was that predicted by a first order (parent) decay equation rather than that of a higher order (daughter) curve; and,

c. radon, astatine, and polonium atoms do not surface ionize to any appreciable extent, requiring any of their isotopes deposited as sources in these experiments to be daughters of francium decay.

Analysis of the gamma data taken with the alpha multiscale revealed two gamma rays of energy 391 and 531 keV with half-lives (1.1 ± 0.4 and 0.7 ± 0.1 seconds, respectively) nearly equal to that of the 6.930 MeV alpha group. These gammas cannot be conclusively assigned to any nucleus at this time. However, the correspondence of the half-lives and energy differences between these gammas and the two alpha groups of ^{206}Fr would indicate they occur within francium astatine, as shown in Figure 19. Gamma-gamma coincidence data taken in these experiments possessed insufficient statistical significance to support or detract from such a scheme, and no levels within ^{202}At or ^{206}Fr have been deduced previously to this study. Thus conclusive evidence must await further experiments.

Using the method outlined in Chapter 3, the alpha branching ratios for ^{206}Fr were determined to be $90.7 \pm 2.3\%$ for the principal alpha group with energy 6.790 MeV and $0.3 \pm 0.2\%$ for the isomer alpha group with energy 6.930 MeV.

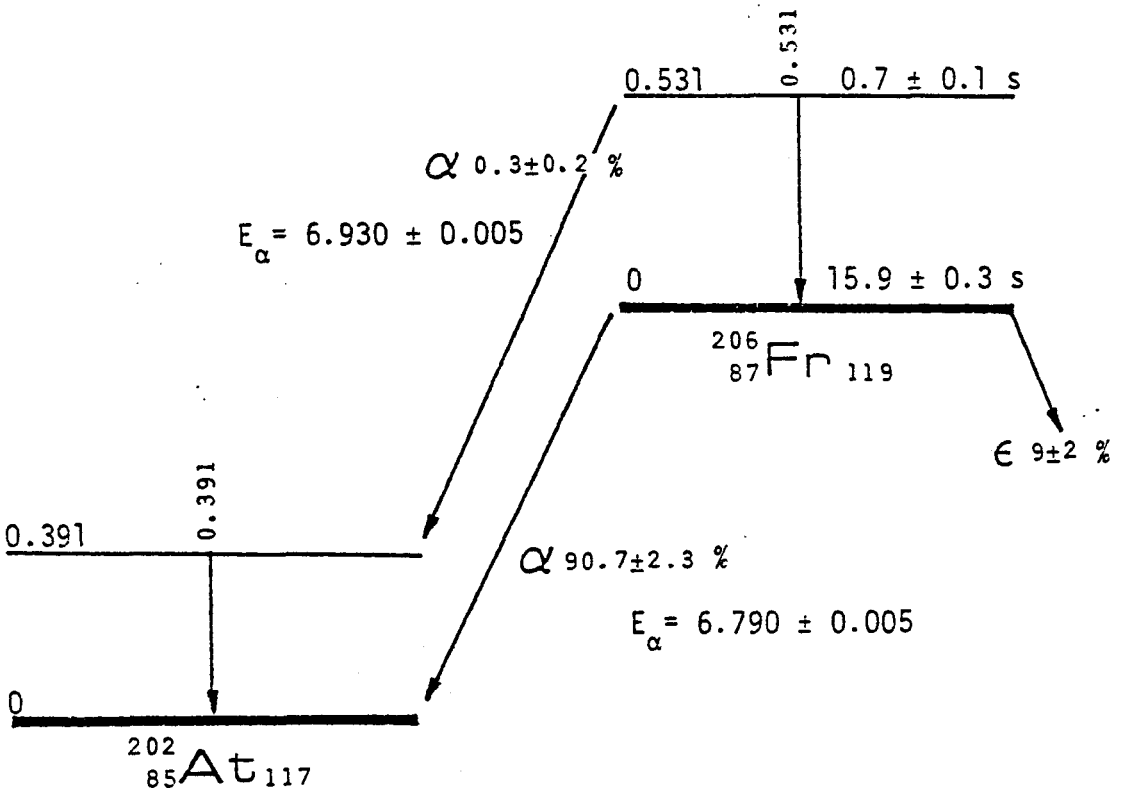

Figure 19. Possible decay scheme for ^{206}Fr showing isomeric level decay. Energies are in MeV.

2. Electron Capture Decay of ^{206}Fr

The electron capture decay populated excited levels in ^{206}Rn which were observed to de-excite through gamma rays with half-lives characteristic of the ^{206}Fr nucleus. The decays of their intensities in the multiscale spectra provided initial evidence for their assignment within radon.

The gamma-gamma coincidence data were taken simultaneously with gamma multiscale data. The summed multiscale data then supplied gating parameters for analyzing the list data. All peaks seen in the summed multiscale data were used as gates to generate coincidence spectra. Those gates on transitions within radon possess x-rays characteristic of radon. These gates shown in Figure 20 and the coincidence relationships found are summarized in Table 6. The gamma-electron coincidence data did not possess significant statistics to permit interpretation.

The gamma and electron singles data permitted the determination of the internal conversion coefficients for the most intense transitions. The electron data disclosed no evidence for any E0 transitions. Overall, statistical error for the ICC's determined in the ^{206}Fr experiments were much higher than in the ^{208}Fr analysis due to the much lower source activities for ^{206}Fr. All transitions were deduced to be M1, E2 or a mixture of these two non-parity changing transitions. Exemplary summed multiscale spectra for the gamma and electron data are shown in Figure 21.

A summary of the data obtained for all transitions within ^{206}Fr is given in Table 7. Energies quoted in that table are from the accurate energies measurements. Intensities listed in the table for the transitions come from the SAMPO analysis of the summed multiscale data.

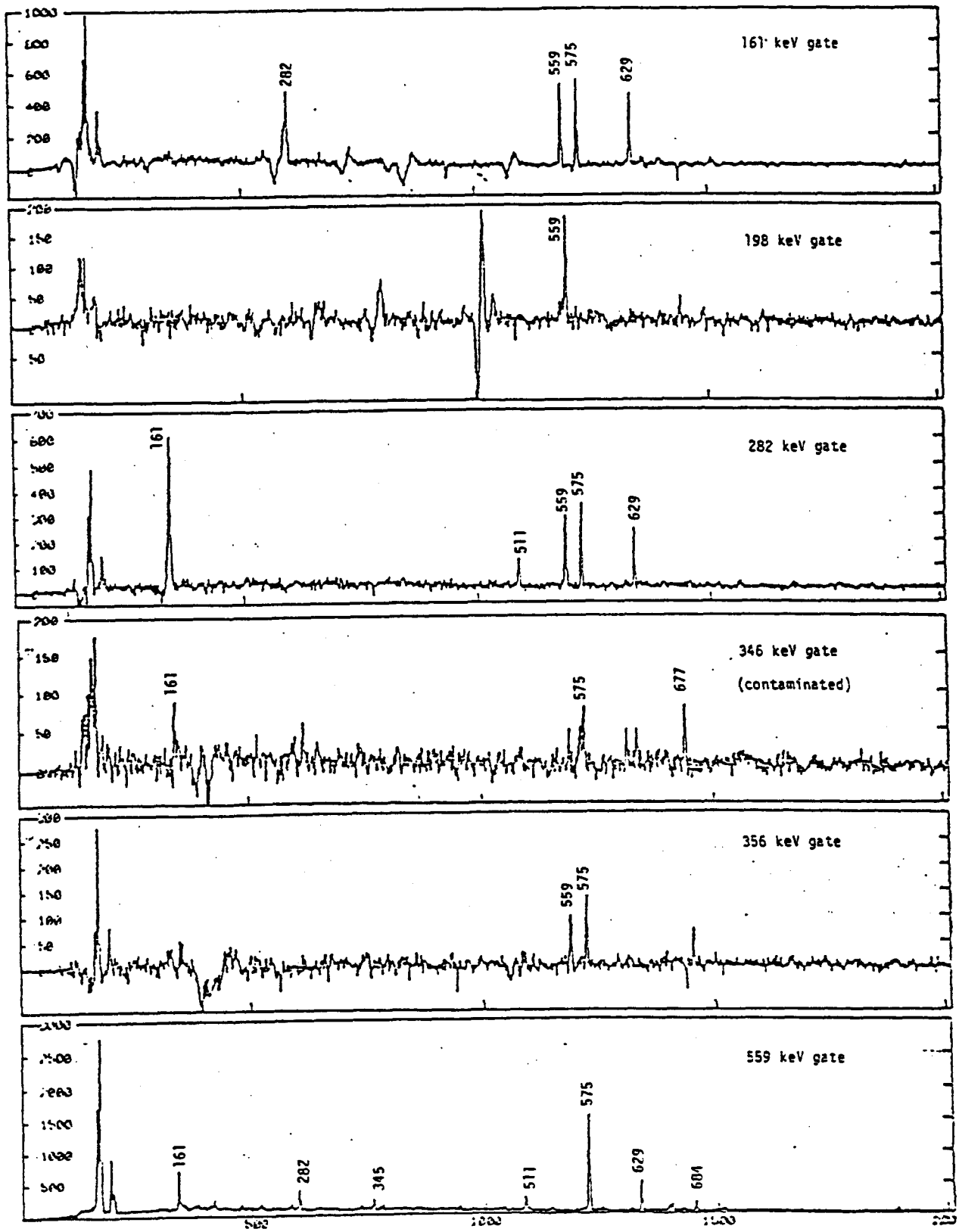

Figure 20. (caption on next page)

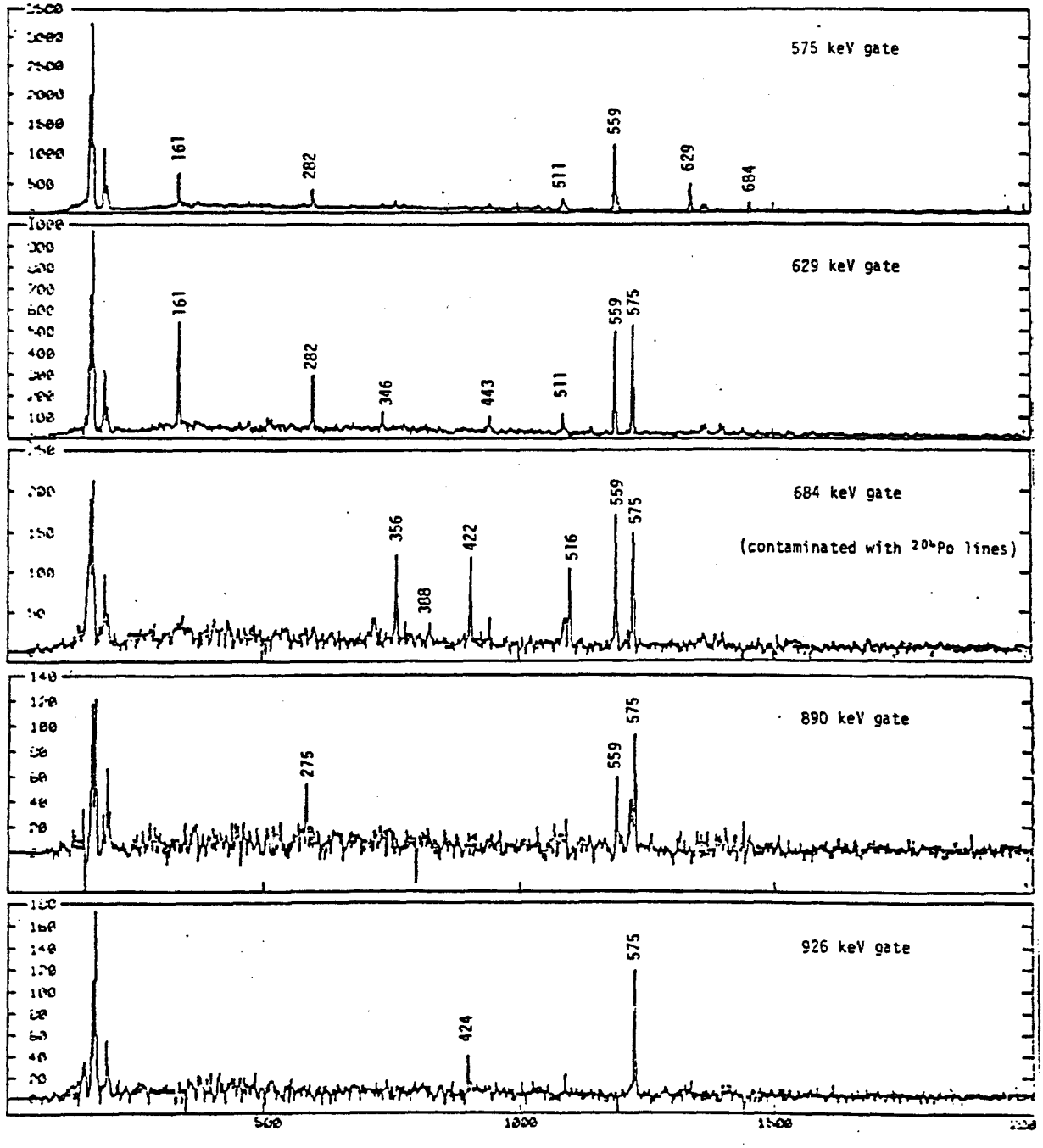

Figure 20 (continued). Gates on transitions in ^{206}Rn. Energies are in keV. The 346 and 684 keV gates are contaminated by lines from other nuclei.

Table 6. Analysis of coincidence gates for ^{206}Rn transitions. "x" denotes appearance of given line in gated spectra.

Gate Energy (keV)	Gamma Energy (keV)												
	161	198	274	283	346	356	559	575	629	684	720	890	926
161				X			X	X	X				
198							X						
283	X						X	X	X				
346	X						X	X	X				
356								X		X			
559								X	X	X		X	
575	X		X	X			X		X	X	X		X
629	X			X	X		X	X					
684					X		X	X					
890				X			X	X					
926								X					

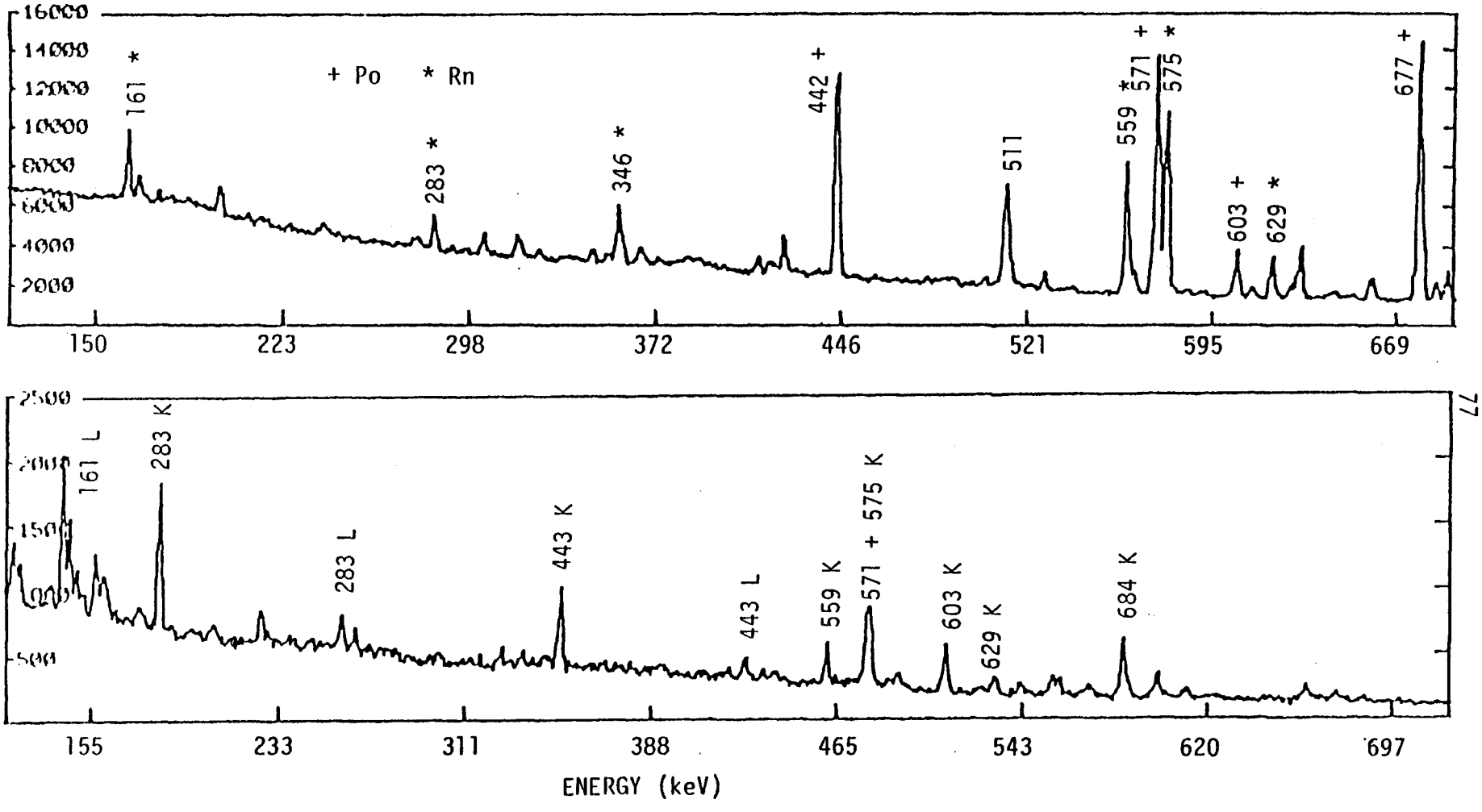

Figure 21. Example of summed multiscale data for decay of ^{206}Fr. The upper figure represents the gamma data while the lower represents the electron data. The strongest lines are identified by energy and element, with energies in keV. No strong transitions were observed beyond the right edge of either figure.

Table 7. Gamma ray transitions observed in ^{206}Rn. Theoretical internal conversion coefficients (ICC's) are from the Hager-Seltzer algorithm.[33] Energies are in keV, and have errors of ±0.1 keV.

Gamma ray Energy	Relative Intensity	shell	ICC (x 10^{-2}) experimental	theoretical	Multi-polarity
161.4	10.0±2.2	L	0.65±0.07	0.681	E2
197.8[1]	4.9±1.0	K	0.34±0.17	0.546	E2
274.9[1]	2.4±0.4				
282.6	8.3±0.9	K	0.51±0.07	0.60	M1
345.6	3.3±1.4				
356.0	3.1±2.0				
559.0	70.0±2.1	K	0.015±0.005	0.019	E2
575.3	100.0	K	0.013±0.005	0.018	E2
628.6	31.0±2.7	K	0.016±0.005	0.015	E2
684.0	8.3±2.1				
890.6	6.1±2.0				
926.5	8.0±2.0				

Notes: 1. Not placed in decay scheme.

Based on this table and the information contained in Figures 20 and 21 and Table 6, the decay scheme shown in Figure 22 was deduced. The ordering of the transitions and levels is based on the observed singles intensities and the results of the accurate energy technique. The scheme was determined to be energy and intensity balanced. Additional confirmation was provided by a coincidence intnesity analysis. The results obtained with the coincidence intensity analysis for several transitions are shown in Table 8.

Since the four gamma cascade from the 1924.3 keV level had been observed previously,[1-3] unique spins and parities were assigned to the 0.0, 575.3, 1134.3, 1762.9, and 1924.3 keV levels. All other spins and parities were delimited by angular momentum restrictions on those transitions for which multipolarities were determined. Since internal gamma feeding within the nucleus does not account for a significant portion of the intensities of the 559.0 and 628.6 keV lines, direct feeding to these levels may be taking place, indicating a spin 5 ground state for ^{206}Fr. Since the ground state of ^{206}Fr has not been measured, such a conclusion must await further experiments for confirmation.

The half-lives of the 8+ and 6+ levels were determined from the TPHC spectra generated by gating on the 282.6 and 161.4 keV gammas and the 161.4 and 628.6 keV gammas, respectively. The TPHC spectra were analyzed using the centroid shift and deconvolution methods. The half-lives found were 6.3 ± 2.4 nsec for the 8+ level and 1.81 ± 1.3 nsec for the 6+ level. The quoted values represent the average for the delayed and anti-delayed TPHC spectra. The quoted error includes an assumed 20% TPHC calibration uncertainty. Sample TPHC spectra and fits to them are shown in Figure 23.

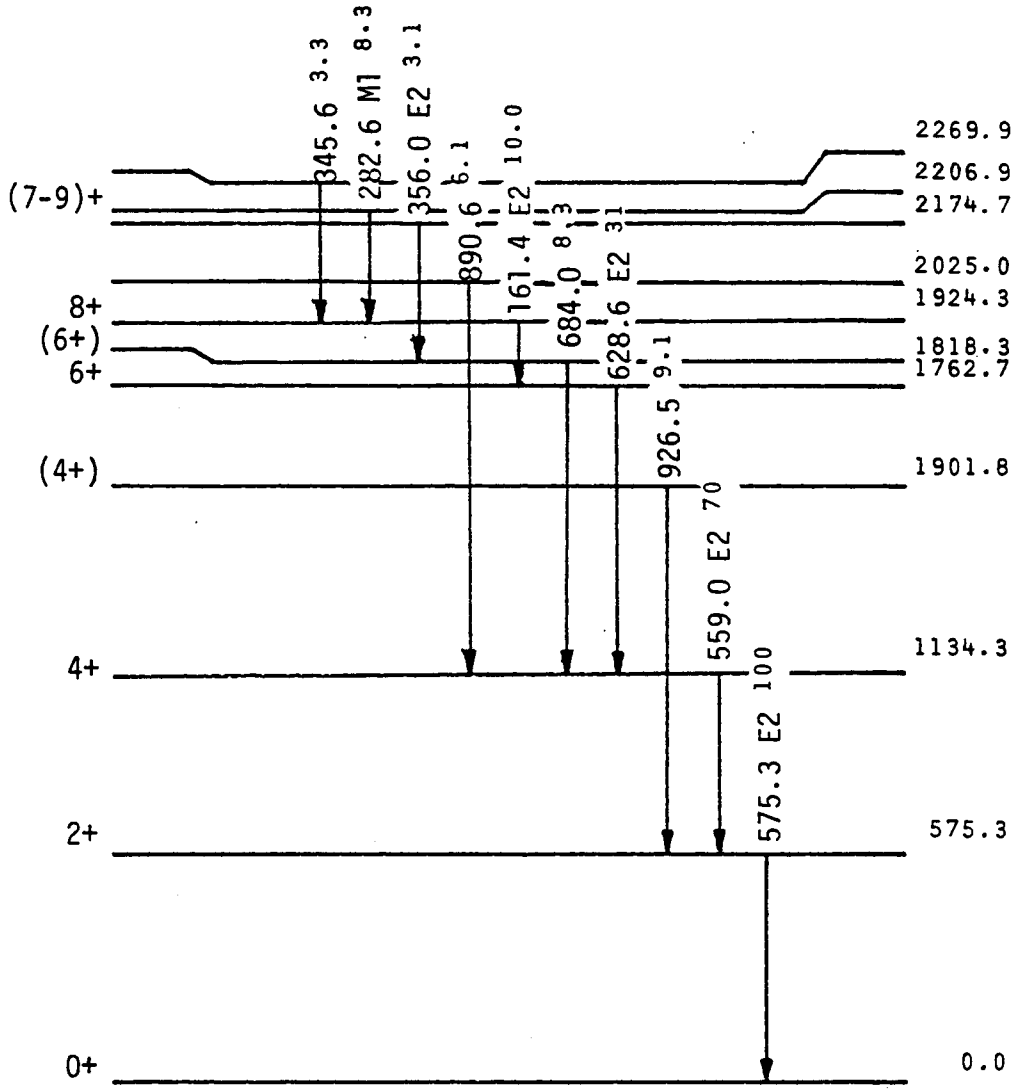

Figure 22. Deduced level scheme for ^{206}Rn. Deduced transition multipolarities are indicated. Small numbers following transition energies denote relative photon intensities.

Table 8. Examples of coincidence intensity analysis for selected ^{206}Rn gates. Energies are in keV; errors are approximately 25% for all intensities.

Gated Energy	Coincident Transition Energy	Relative Intensity in Gate	Relative Intensity in Gate Calculated from Decay Scheme
282	161	84	100
	511	35	-
	559	90	100
	575	100	100
	629	77	100
629	161	26	31
	282	23	23
	511	15	-
	559	100	100
	575	97	100
684	356	36	37
	559	100	100
	575	88	100

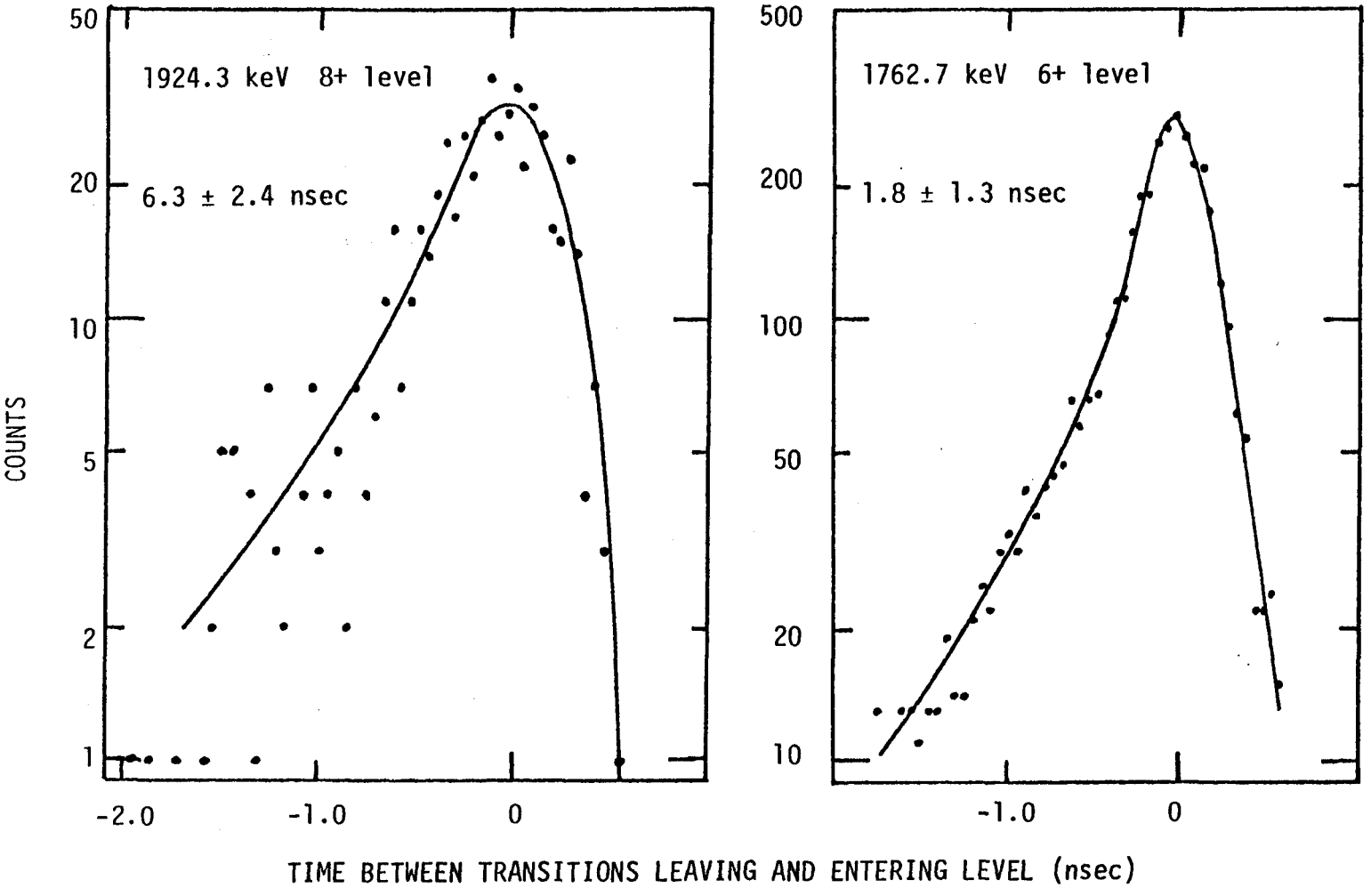

Figure 23. Sample TPHC spectra used to determine half-lives of 8+ and 6+ levels in ^{206}Rn. Fitting spectra are indicated by lines. Values for half-lives shown in the figures are based on averages of both delayed and anti-delayed spectra.

CHAPTER 5

DISCUSSION OF RESULTS AND CONCLUSIONS

A. Comparison of Results with Previous Work

1. Alpha Decay Properties of $^{205-208}Fr$

In addition to the alpha decay measurements made for $^{206,208}Fr$, alpha decay measurements also were made for $^{205,207}Fr$ using the method described in Chapter 3. The values obtained for the energy, half-life and alpha branching ratio for each isotope are given in Table 9. The table also shows results obtained for the alpha branching ratios by other experimenters, Hornshoj et al.[10]

All experimentally deduced alpha branching ratios are observed to be somewhat higher than those previously reported. It is not possible to ascertain the exact cause of these differences from previous values by an examination of the information contained in references 10 and 11. However, it should again be noted that the measurement method used here does not rely on accurate knowledge of the daughter alpha branching ratios, while the method used by Hornshoj et al. does. A supposition from this difference in technique would be that the values for the daughter alpha branching ratios used by them were inaccurate. Further experiments would be needed to support this as a possible explanation for the discrepancies.

The final column in Table 9 shows the alpha decay reduced width calculated with the formalism of Rasmussen.[44] In this formalism,

Table 9. Summary of results of alpha measurements and reduced width calculations for francium nuclei, A = 205-208. Energies are in MeV, with ±0.005 MeV error for all energies.

Mass	Energy	Half-life (sec)	α branching ratio measurement this study	previous (ref. 10)	angular momentum transfer (ħ)[1]	reduced width (x 10^{-2})
208	6.636	58.1±0.3	88.8±2.8	74±3	2	0.507±0.030
207	6.766	14.9±0.1	98.6±1.0	93±3	0	4.31±0.42
206^{m}	6.930	0.7±0.1	0.3±0.2	-	-	-
206	6.790	15.9±0.3	90.7±2.3	85±2	2	0.561±0.016
205	6.917	3.9±0.1	∿100	-	0	4.8±0.2

Notes: 1. Angular momentum transfer is based on ground state spin differences deduced from the Evaluated Nuclear Structure Data File, Oak Ridge National Laboratory, August 1979.

alpha particle decay constants are expressed in terms of reduced width δ^2 such that

$$\delta^2 = \frac{\lambda_p}{P} h$$

where λ_p is the alpha decay partial decay constant and P the penetrability of the nuclear potential barrier. The barrier penetrability for an isotopic series of nuclei should be nearly the same for each nucleus since much of the barrier height depends solely on the coulombic forces. Reductions in the partial half-life for the nucleus caused by a hindering effect on the decay would be reflected in a lower reduced width. In the Rasmussen formalism, P incorporates an angular momentum barrier with a Woods-Saxon form for the nuclear potential.

The calculated reduced widths given in Table 9 may be compared with those for the primary alpha decay groups of the neighboring even-even radon and radium nuclei. Even-even nuclei (with 0^+ ground states) that alpha decay obviously decay to other even-even nuclei, with the primary alpha group connecting the ground states of the parent and daughter nuclei. These even-even to even-even alpha decays represent useful reference points for unhindered decays. This is because no angular momentum change takes place in these decays and paired nucleons are contained in the parent nuclei which may be used to construct an alpha particle.

The results of such a comparison are shown in Figure 24 for the reduced widths given in Table 9. The even N francium nuclei do not appear to be hindered, while the odd N nuclei exhibit appreciably lower reduced widths. This phenomenon can be explained by considering probable schemes for alpha particle formation in the nucleus. Possibly only paired protons in the parent nucleus are used as the charged

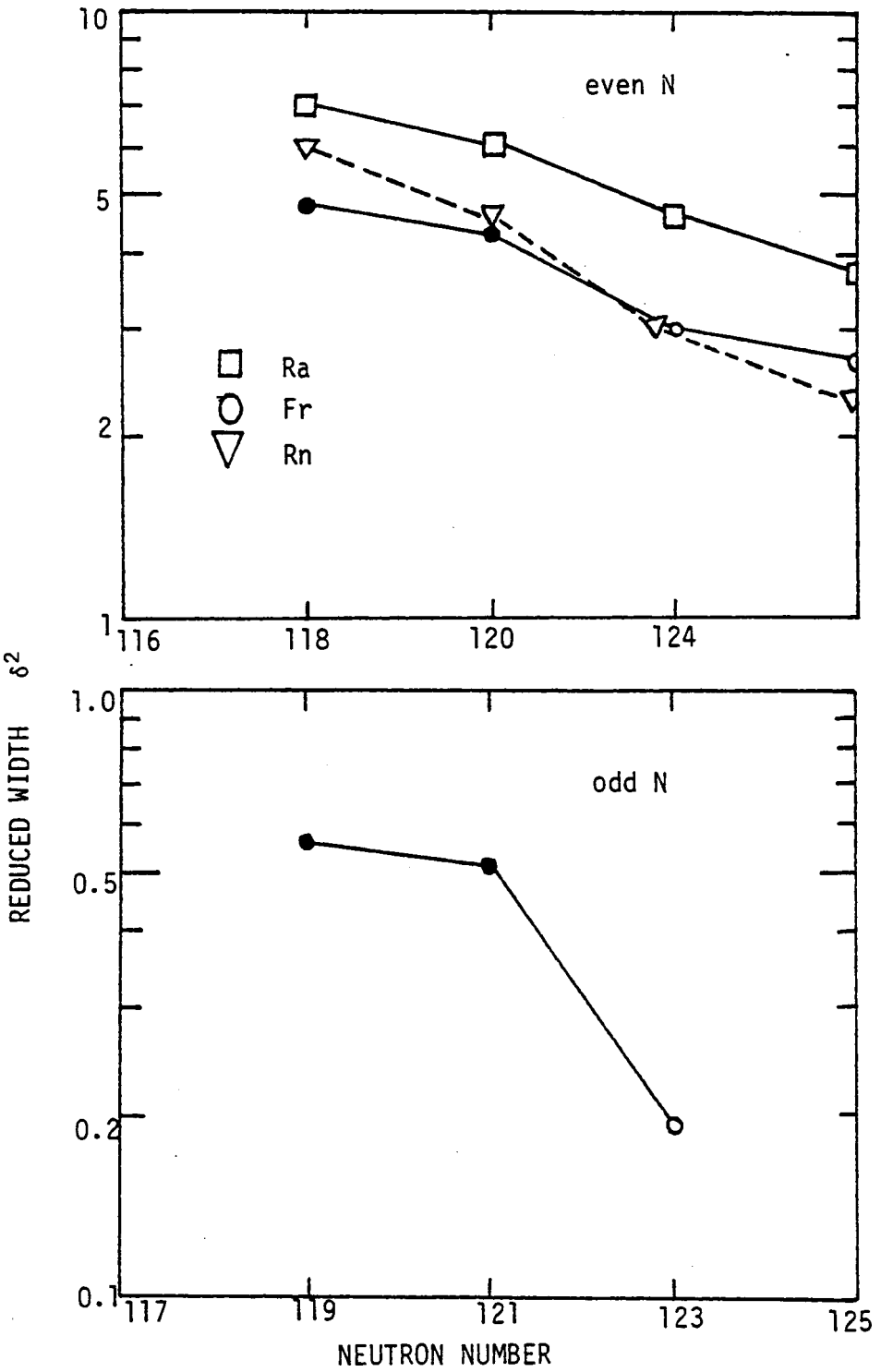

Figure 24. Reduced widths for radon, francium, and radium isotopes with 116 < N < 124. Darkened circles represent results given in Table 9. Other data shown is from K. S. Toth (private communication).

constituents of the alpha particle. However, with the odd neutron particle francium isotopes, the neutron constituents could be assembled by braking a neutron pair and coupling one member of the pair to the odd neutron. Such pair breaking would result in a decreasing penetrability and, consequently, a higher reduced width.

Another explanation[45] for the hinderance of alpha decays in odd-nucleon nuclei assumes the alpha particle does not use the odd nucleons. Instead pairs are removed from "beneath" the odd nucleons with hindering effects only observed when the odd nucleons must change to different quantum states. If the spherical shell model configuration for the nuclei connected by the francium alpha decays are considered, the neutrons and protons in both parent and daughter would be $h_{9/2}$ and $i_{13/2}$, with no change in quantum state occurring. The experimental data in Figure 24 would, if interpreted by this theory, indicate no change in the proton quantum states, but a definite change in the neutron quantum states. Such an interpretation would indicate that the nuclei are deformed rather than spherical. Experimental data on the nuclear shapes of these nuclei do not exist at this time, so such an interpretation cannot be verified.

2. Level Schemes for ^{206}Rn and ^{208}Rn

The deduced level scheme for ^{206}Rn confirms unequivocally the energies for the first four levels determined by Horn et al.,[3] shown earlier in Figure 1 (page 5). The precision to which the transition energies have been determined in this study is considerably greater than all previous work, and the level structure below the 8^+ isomer has been given more detail.

The measurement of the 8^+ half-life here conflicts with those previously deduced. Horn et al. used the slope method alone to determine the 8^+ lifetime without correcting for the finite resolving time of their coincidence system, which was roughly the same order as the half-life being measured.[46] This would result in a higher than actual value for the level lifetime. The methods used by the other two groups[1,2] were not described, so possible explanations of the conflicting values cannot be made. The 6^+ level lifetime has not been determined previously.

The level structure of ^{208}Rn has been greatly extended beyond that shown in Figure 2 (page 6) from Backe et al.[2] This detail is essential for comparison with the theoretical predictions by the IBA, as will be seen below. Though there is considerable uncertainty in the measurement of the 8^+ lifetime provided by this series of experiments, the value obtained supports that made by Backe et al.

B. Systematics of the Radon Nuclei, $N \leq 126$

Figure 25 shows the systematic trends of the levels observed in-beam in the even radon nuclei from the closed shell nucleus ^{212}Rn to ^{204}Rn. The schemes are taken from reference 2, with the A = 206 levels ordered according to the results of this work.

The isomeric 8^+ level is seen to rise with a generally decreasing lifetime. The B(E2) values for this transition may be calculated for A = 204, 206, 208, and 212; the B(E2) for A = 210 cannot be determined since the $8^+ \rightarrow 6^+$ transition energy is unknown. These values are shown on Figure 25. These states can be interpreted[47] to be four particle states--four $h_{9/2}$ proton particles outside the closed ^{208}Pb

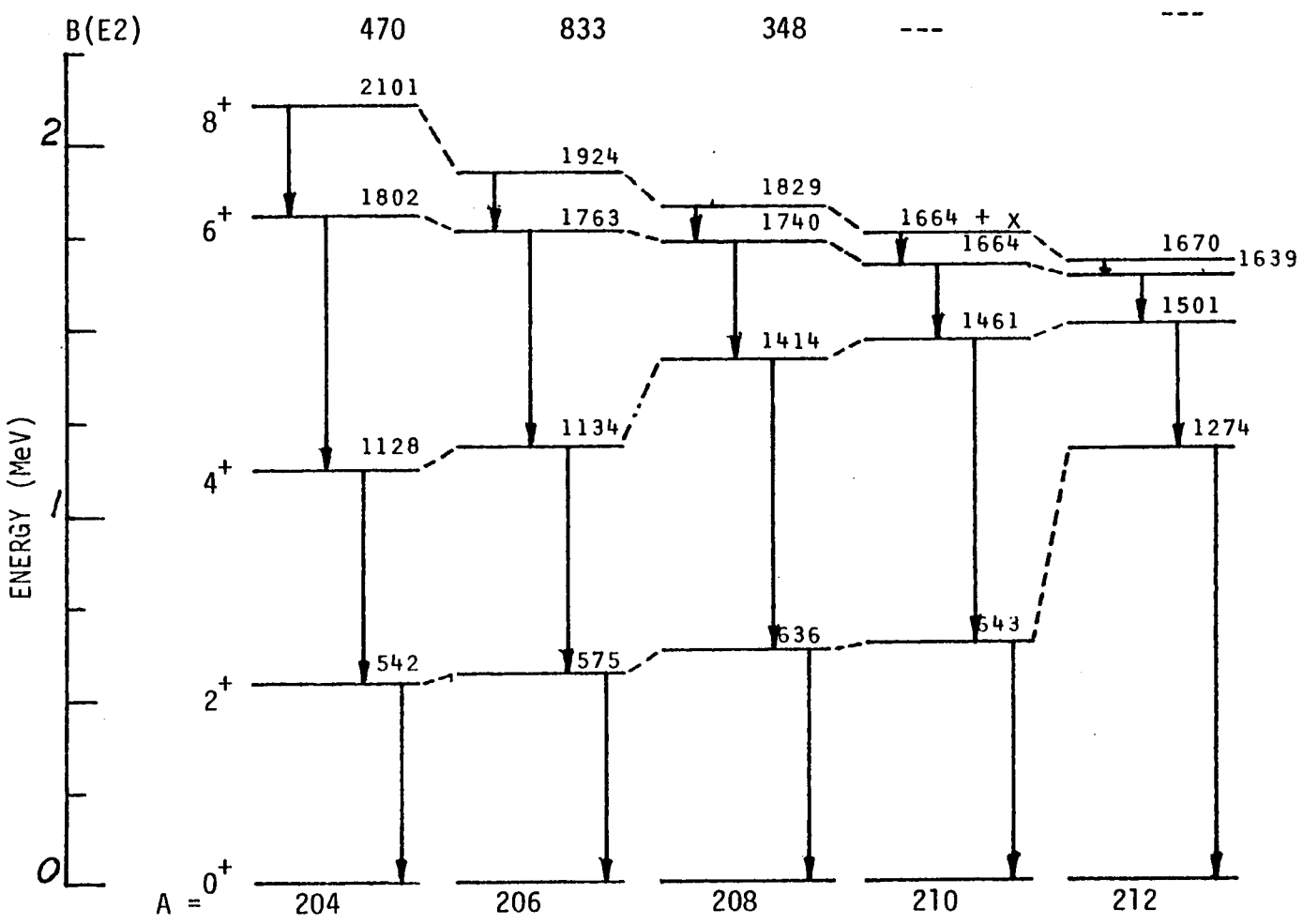

Figure 25. Systematic trends of levels populated by in-beam experiments for even A, neutron deficient radon isotopes. B(E2) values for the 8+ → 6+ transition are shown, in units of e^2fm^4. A = 204 and 206 values from this study; other information from reference 2.

core coupled to 8^+--since the state appears to be nearly unaffected by neutron number. Such an interpretation has been applied to the 8^+ levels in even A, neutron deficient polonium isotopes.[48]

Figure 26 shows more detailed systematics for ^{206,208}Rn made possible by these experiments. A comparison of this figure with Figure 25 reveals that the lower 4^+ is populated in ^{206}Rn but not in ^{208}Rn. The lowest 4^+ is by definition the 4^+ yrast state and should be populated by in-beam experiments. This difference in population may denote a rotational band crossing.[49]

Figure 26 also shows similarities in which the ground state band populated by in-beam studies de-excites in decay studies. In both nuclei an initial strong M1 transiton not observed in-beam feeds the 8^+ isomer, which in turn de-excited by a series of four strong E2 transitions. However, it may be possible to consider the ^{208}Rn nucleus as exhibiting shape co-existence. In-beam studies of ^{206}Po, which has a very similar level structure to ^{208}Rn, have given evidence of a 2^+ level lying below the lower 4^+ level in that nucleus.[50] If such a state existed in ^{208}Rn, the presence of a side rotational band might be implied, consisting of that level and the 1414 (4^+), 1740 (6^+), and 1829 (8^+) keV levels. This would provide a possible explanation in terms of band crossing, with the crossing bypassing the side band 2^+. Such an explanation must await the confirmation of such a 2^+ level in ^{208}Rn for support.

In light of the fact that in-beam studies generally populate the more collective nuclear states, the lower 4^+ in ^{206}Rn would appear to be less collective than the uppermost. But collective states generally are depressed below non-collective states with the same angular

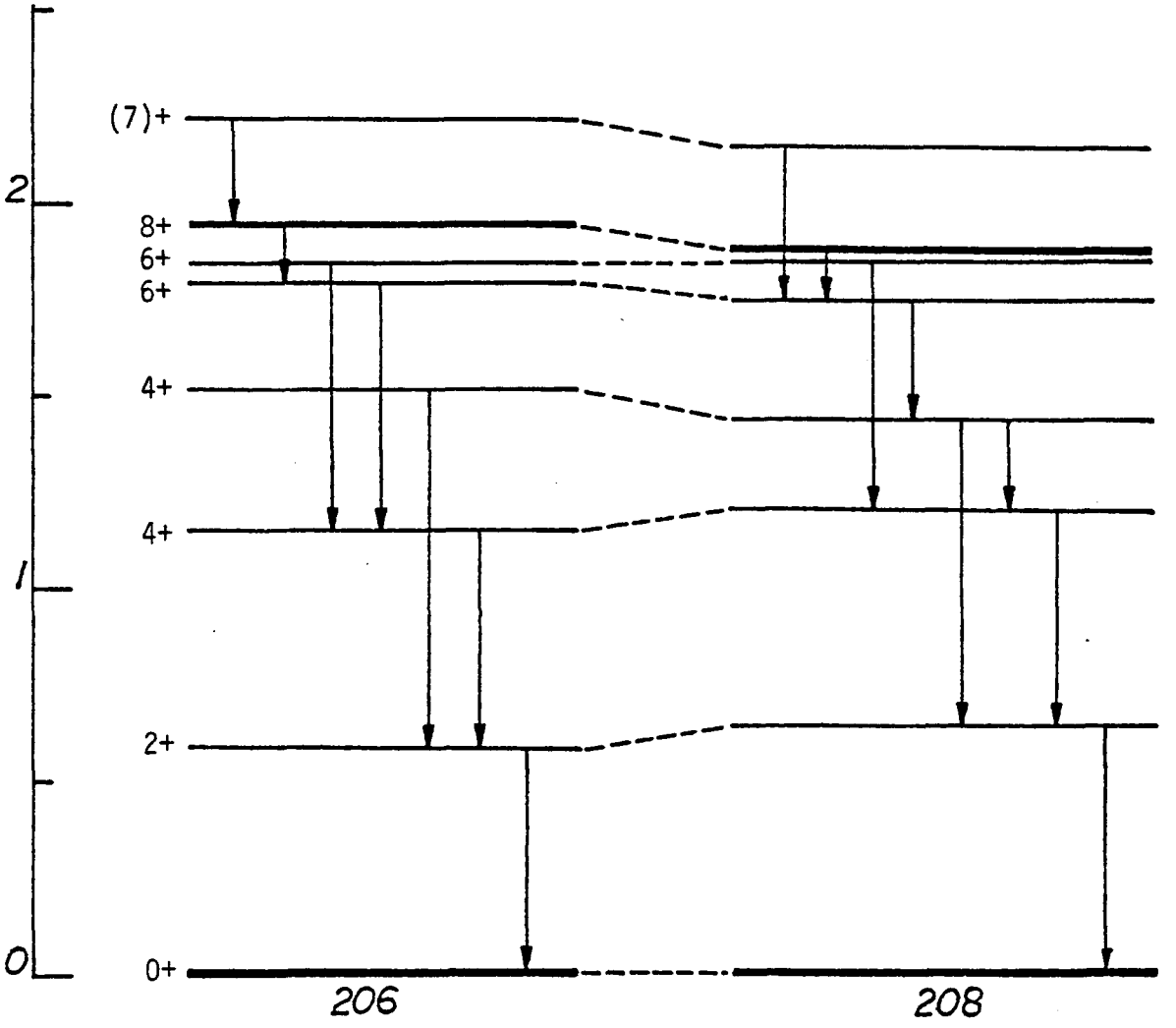

Figure 26. Detail of level schemes of ^{206}Rn and ^{208}Rn, showing systematic trends of levels populated in the decays of the francium parents. Energies are in MeV. The spins given are either those determined for the levels shown or represent best estimates.

momentum, so such an interpretation seems unlikely. Horn and co-workers plan to investigate ^{208}Rn in-beam in the future.[46] It will be interesting to see if the lower 4^+ level indeed is not populated by in-beam reactions or some problem prevented Backe et al. from observing it. At this time, this 4^+ level paradox remains unresolved.

C. IBA Calculations for Nuclei, $N \leq 122$

One purpose of this study was to test the interacting boson approximation in the region $Z > 82$, $N < 126$. As mentioned in the Introduction, such a test necessitates having detailed knowledge of the level structures of the nuclei to be studied. The results of this study permit a reasonable first step towards judging the validity of the model in this region.

As a first approximation to a description of the more detailed level scheme of ^{208}Rn the analytical expressions in equations 2.3 (page 17), 2.6 (page 22), and 2.8 (page 24) were applied to the spectrum. This nucleus, with four protons and four neutron holes outside the ^{208}Pb core, would have four bosons. When these limit formulae were applied, only the SU(5) equation 2.3 could properly order the levels observed experimentally by energy and spin. The 8^+ level was not included in these or subsequent calculations since its four particle nature would preclude an explanation of that state as the four d-boson, 8^+ level in an IBA description.

Using these initial SU(5) parameters, the computer program PHINT was used to calculate the theoretical spectrum using the full IBA Hamiltonian of equation 2.2. The program allows the computer to vary the nine parameters of equation 2.2 to minimize the chi-square

difference between the experimental and theoretical spectra. In the analysis used in this study, initially only the 0^+, 2^+, 4^+, and 6^+ levels were fit.

It was found that only five of the nine parameters are needed to achieve good agreement between theory and experiment for ^{208}Rn. These five parameters are the four SU(5) parameters noted in the discussion of equation 2.3 (ε_d, c_0, c_2, and c_4) and the coefficient for the term

$$(d^+d^+)^{(0)}\ (ss)^{(0)} \ + \ (dd)^{(0)}\ (s^+s^+)^{(0)}$$

henceforth called G. The theoretical spectrum obtained is compared with the experimental spectrum in Figure 27. It is seen that the theoretical spectrum shows very good agreement with the observed spectrum, correctly predicting the known spins for the low lying states or predicting parities within the range of possible spins. Many more low spin states are predicted than are observed. The presence of these states cannot be ruled out based on this study and additional efforts to find them must await further in-beam and decay studies.

Above the energy of the 8^+ isomeric level the level density can be seen to increase significantly in ^{208}Rn. Such an increase generally occurs as a critical energy is reached above which non-collective effects dominate collective ones. In particular, at this energy it may be possible to break the closed core and excite nucleons from it. Since the IBA requires that boson number be conserved, spectra above this critical energy are not explicable in terms of the model. The IBA only predicts one state above this point, the 8^+ level, which appears to be found in the experimental spectra.

^{208}Rn

Experimental results IBA calculations

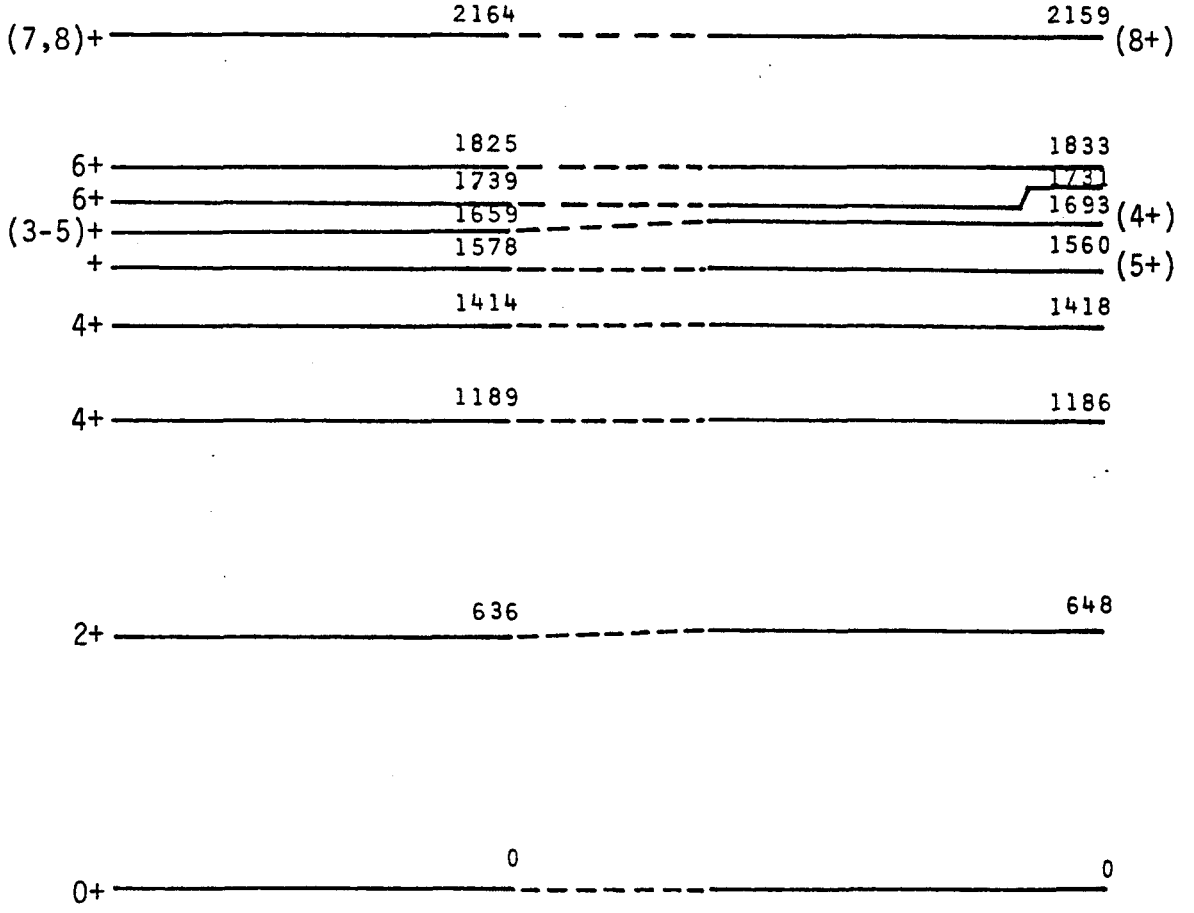

Figure 27. Comparison of deduced level scheme for ^{208}Rn with the results of the IBA calculations. Model parameters are given in Table 10. Energies are in keV. Only IBA levels which correspond to experimental levels are shown.

There is insufficient information at this time to compare predictions of the IBA to experiment for electromagnetic transitions. It can be noted, however, that the 778 keV, $4_2^+ \rightarrow 2^+$ transition is ruled out by the model. As can be seen from the selection rules for E2 transitions, equation 2.12 (page 27), the number of d bosons in a nucleus cannot change by 2 with an E2 transition. However, the 4_2^+ state is an $n_d = 3$ state, while the 2^+ state is an $n_d = 1$ state. This state presents an important problem in interpreting the observed ^{208}Rn level scheme in terms of the IBA. Two possible explanations can be considered: (a) the level may not be an IBA state, or (b) it may represent a new mode of excitation within the model, a $J^\pi = 4^+$ or "g"-boson. A definite conclusion concerning the nature of this state must await further experiments.

The level scheme deduced for ^{206}Rn in this study and that deduced for ^{204}Rn by Backe et al.[2] do not yet possess sufficient detail to permit as detailed a study of their structures with the IBA as is possible for ^{208}Rn. Figure 28 shows the results of the IBA calculations performed for those nuclei using PHINT. For those levels deduced in the two nuclei, good agreement exists between theory and experiment. However, much greater detail in these two level schemes, particularly ^{204}Rn, is mandatory if conclusions concerning the applicability of the IBA to these nuclei are to be made. Also, as in the case of ^{208}Rn, electromagnetic transitions cannot be analyzed at this time to correlate theory and experiment for these two nuclei.

The IBA Hamiltonian parameters used for these three nuclei are given in Table 10. The parameters are seen to vary smoothly, as is normally observed in series of nuclei.[18] The d boson energy of

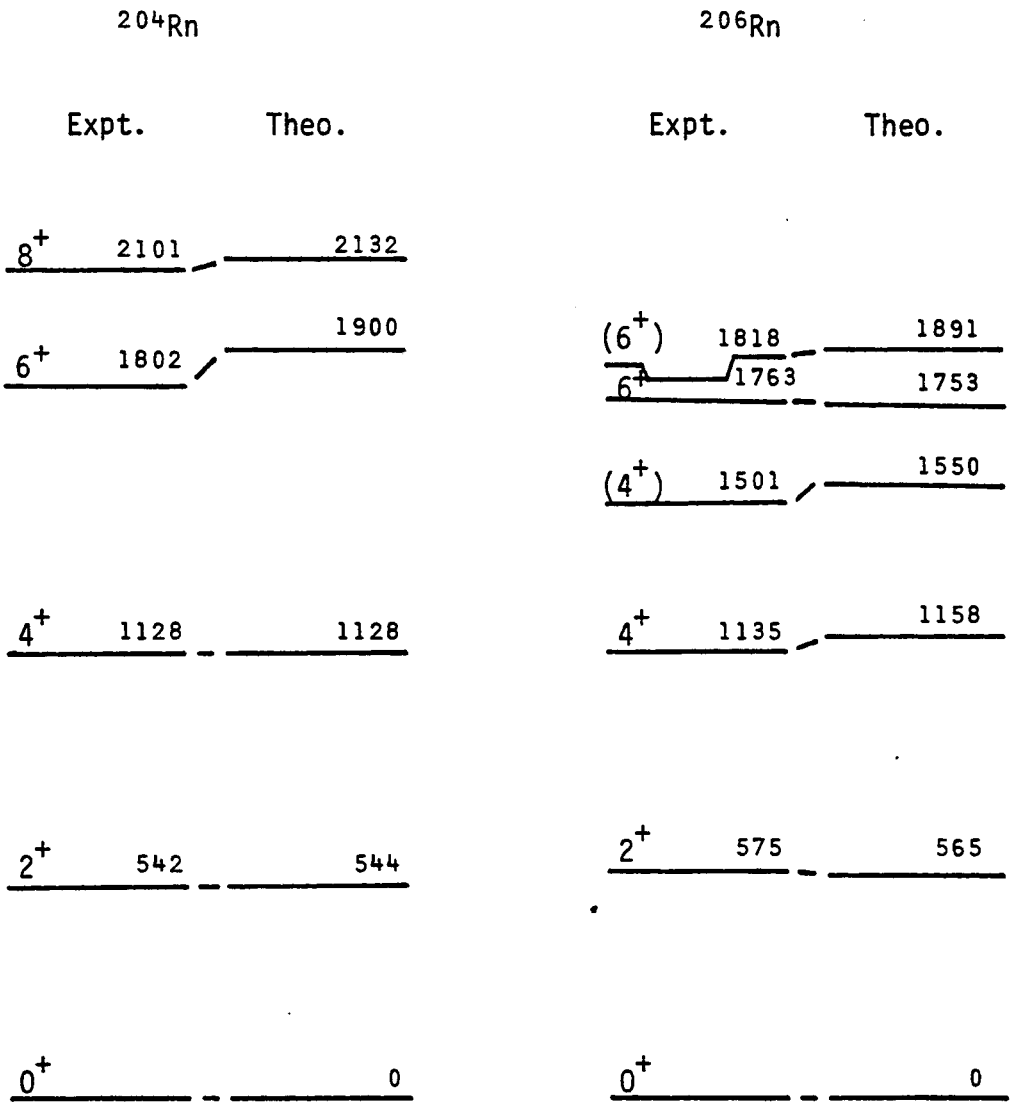

Figure 28. Comparison of deduced level schemes for ^{204}Rn and ^{206}Rn with the results of IBA calculations. The ^{204}Rn level scheme is from Backe et al.[2] Parameters used are given in Table 10.

Table 10. Parameters used in IBA Hamiltonian for neutron deficient radon nuclei with A = 204, 206, and 208. Energies are in keV.

Parameter	Mass number 204	206	208
ε_d	534.3	540.8	580.6
c_0	20.6	- 17.5	-358.5
c_2	-222.9	-236.4	-309.3
c_4	- 32.1	- 22.5	-109.7
G	-108.6	-100.0	- 93.1

slightly over 0.5 MeV is suggestive of J = 2 two nucleon coupling energies, such as those shown in Figure 3 (page 11). This might be expected if the bosons are indeed two nucleon couplings.

D. Future Directions for Study

From the discussion above, it is seen that many "good experiments" remain to be performed in the neutron deficient region above Z = 82. In this section some possible experiments are suggested to further expand knowledge of this region.

An important test of the IBA in this region has been performed by comparing the model calculations for the energies of the levels to the experimental spectra. A much more stringent test would be possible if the electromagnetic transition probabilities for several transitions in each nucleus were determined experimentally for comparison to the theory. A series of experiments designed for this purpose would be very useful.

Further level structure detail would make model comparisons more complete, particularly for the ^{204}Rn and ^{206}Rn nuclei. This detail could be achieved by conducting more gamma-gamma and electron-gamma coincidence experiments than time has permitted for this study. Such experiments would allow the deduction of more levels. Additionally, with simultaneous multiscaling during the electron-gamma coincidence experiments, internal conversion coefficients could be determined. These could fix or delimit the spins and parities for more of the deduced levels.

For the francium parent nuclei studied here, several more measurements could help illuminate their properties further. The fast atomic

beam facility under development by Carter et al. at UNISOR may permit the measurement of the francium ground state spins for A < 208. Determination of the ^{206}Fr ground state spin would help delimit the spins and parities of the fed levels in the daughter nuclei. The production rates for ^{206}Fr and its possible spin of 5 make the measurements of its ground state spin marginally possible.[53] Any definite conclusions on the feasibility of these experiments must await the initial tests of the facility, tentatively scheduled[53] for October 1980.

The isomeric state of ^{206}Fr proposed in this study could be confirmed by additional experiments. Two approaches are possible at the UNISOR facility. The most feasible would be to perform an alpha-gamma coincidence experiment to determine the coincident gamma transitions associated with the short-lived isomer. A marginally feasible experiment would involve creating ^{206}Ra as a parent nucleus to decay to levels in ^{206}Fr. It is not known at this time if ^{206}Ra electron capture or positron decays to ^{206}Fr. Additional problems with any decay studies include the very short half-life of ^{206}Ra (0.4) sec) and ion beam/target material matching. Thus, only the alpha-gamma coincidence method offers much hope of determining the existence of the isomeric level in ^{206}Fr by UNISOR experiment. In-beam studies may illuminate this nucleus more thoroughly.

Besides the experimental studies of the region mentioned above, further theoretical studies of the neutron deficient radons would be useful in interpreting the observed phenomena. The boson expansion technique of Tamura, Kishimoto, and Kammuri[54-56] was applied to the ^{208}Rn level scheme but was unsuccessful.[57] Further extensions of that

model are planned and may result in better agreement with experiment.[57] A truncated shell model calculation is planned by J. B. McGrory[58] using the truncation scheme formulated by him and others.[59] The neutron-proton boson model[23] may be applied to the neutron deficient radon nuclei provided more detail on the level structures is obtained. All of these theoretical approaches will increase understanding of this region, if attempted, whether successful or not.

REFERENCES

1. T. Inamura, S. Nagamiya, A. Hashizume, Y. Tendow, A. Katou, IPCR Cyclotron Progress Report 4, 67 (1970).

2. H. Backe, Y. Gono, E. Kankeleit, L. Richter, F. Weik, and R. Willwater, Jahresbericht, Max Planck Institute (Heidelberg), 123 (1977).

3. D. Horn, C. Baktash, and C. J. Lister, Bull. Amer. Phys. Soc. 24, 837 (1979).

4. T. Kempistry, A. Korman, T. Morek, L. K. Peker, Z. Haratym, S. Chojnacki, JINR P6, 6725 (1972).

5. A. Arima and F. Iachello, Ann. Phys. (N.Y.) 99, 253 (1976).

6. A. Arima and F. Iachello, Ann. Phys. (N.Y.) 111, 201 (1978).

7. O. Scholten, F. Iachello, and A. Arima, Ann. Phys. (N.Y.) 115 321 (1978).

8. A. Arima and F. Iachello, Phys. Rev. Lett. 35, 1069 (1975).

9. A. Arima and F. Iachello, Phys. Rev. Lett. 40, 385 (1978).

10. K. Valli, E. K. Hyde, J. Inorg. Nucl. Chem. 29, 2503 (1967).

11. P. Hornshoj, P. G. Hansen, B. Jonson, Nucl. Phys. A230, 365 (1974).

12. A. Bohr, Mat. Fys. Medd. Dan. Vid. Selsk. 27, No. 14 (1952).

13. A. Bohr and B. R. Mottelson, Mat. Fys. Medd. Dan. Vid Selsk. 27, No. 16 (1953).

14. S. T. Belyaev, Mat. Fys. Medd. 31, 11 (1959).

15. J. Bardeen, L. N. Cooper, and J. R. Schrieffer, Phys. Rev. 106, 162 (1957).

16. T. T. S. Kuo and G. E. Brown, Nucl. Phys. 85, 40 (1966).

17. T. T. S. Kuo and G. E. Brown, Nucl. Phys. A114, 241 (1968).

18. F. Iachello in Interacting Bosons in Nuclear Physics, ed. by F. Iachello (Plenum, New York, 1979), pp. 1-16.

19. J. P. Elliott, Proc. Roy. Soc. 245, 128 (1958).

20. M. Moshinsky, Notas de Fisica 2, 255 (1979).

21. L. Wilets and M. Jean, Phys. Rev. 102, 788 (1956).

22. F. Iachello and O. Scholten, Phys. Rev. Lett. 43, 679 (1979).

23. O. Scholten in Interacting Bosons in Nuclear Physics, ed. by F. Iachello (Plenum, New York, 1979), pp. 17-35.

24. J. N. Ginocchio, Phys. Lett. 79B, 173 (1978).

25. T. Otsuka, A. Arima, F. Iachello, I. Talmi, Phys. Lett. 76B, 139 (1978).

26. T. Otsuka, A. Arima, and F. Iachello, Nucl. Phys. A309, 1 (1978).

27. D. R. Bes and R. A. Broglia, in Interacting Bosins in Nuclear Physics, ed. by F. Iachello (Plenum, New York, 1979), pp. 143-150.

28. R. V. Jolos, F. Donau, and D. Janssen, Teor. Mat. Fys. 20, 112 (1974).

29. S. G. Lie and G. Holzwarth, Phys. Rev. C12, 1035 (1975).

30. T. Kishimoto and T. Tamura, Nucl. Phys. A192, 246 (1972).

31. F. Plasil, ORNL/TM-6054 (1977).

32. H. K. Carter, E. H. Spejewski, R. L. Mlekodaj, A. G. Schmidt, F. T. Avignone, C. R. Bingham, R. A. Braga, J. D. Cole, A. V. Ramayya, J. H. Hamilton, E. L. Robinson, K. S. R. Sastry, and E. F. Zganjar, Nucl. Instr. and Meth. 139, 349 (1976).

33. R. S. Hager and E. C. Seltzer, Nucl. Data A4, 1 (1968).

34. B. G. Ritchie, Masters Thesis, University of South Carolina (1975).

35. E. DeLima, H. Kawakami, A. DeLima, R. Hichwa, A. V. Ramayya, J. H. Hamilton, W. Dunn, and H. J. Kim, Nucl. Instr. and Meth. 151, 221 (1978).

36. Z. Bay, Phys. Rev. 77, 491 (1950).

37. Developed by M. L. Halbert, ORNL (1976).

38. H. H. Jorch and J. L. Campbell, Nucl. Instr. and Meth. 143, 551 (1977).

39. J. T. Routti and S. G. Prussan, Nucl. Instr. and Meth. 72, 125 (1969), revised by J. D. Cole and Ir. Lourens.

40. R. J. Gehrke, J. E. Cline, and R. L. Heath, Nucl. Instr. and Meth. 91, 349 (1971).

41. K. Debertin and U. Schotzig, Nucl. Instr. and Meth. 158, 471 (1979).

42. C. Ekstrom, S. Ingleman, G. Wannberg, and M. Skarestad, Physica Scripta 18, 51 (1978).

43. R. D. Griffioen and R. D. MacFarlane, Phys. Rev. 133, 1373 (1964).

44. J. O. Rasmussen, Phys. Rev. 115, 1675 (1959).

45. M. A. Preston and B. K. Bhaduri, Structure of the Nucleus (Addison-Wesley, Reading, MA, 1975), p. 531.

46. D. Horn, private communication, October, 1979.

47. T. Kenpistry, A. Korman, T. Morek, L. K. Peker, Z. Horatym, and S.Chojnacki, J.I.N.R. P6, 6725 (1972).

48. T. Yamazaki, Phys. Rev. C1, 290 (1970).

49. I. Y. Lee, private communication, October, 1979.

50. I. Bergstrom, J. Blomqvist, and C. J. Herrlander, The Jyvaskyla-Stockholm Collaboration-Res. Inst. Phys., Stockholm, Ann. Rept., 119 (1976).

51. Olaf Scholten, Kernfysisch Vernsneller Instituut, 1978.

52. H. K. Carter, C. R. Bingham, in Proceedings of the International Symposium on Future Directions in Studies of Nuclei Far From Stability, ed. by J. H. Hamilton (to be published).

53. H. K. Carter, private communication, November, 1979.

54. T. Kammuri and T. Kishimoto, Z. Physik A276, 51 (1976).

55. T. Kammuri and T. Kishimoto, Z. Physik A278, 41 (1976).

56. T. Kishimoto and T. Tamua, Nucl. Phys. A192, 246 (1972).

57. K. Weeks, private communication, September, 1979.

58. J. B. McGrory, private communication, June, 1979.

59. K. T. Hecht, J. B. McGrory, and J. P. Draayer, Nucl. Phys. A197, 369 (1972).